Supplementary Material

Exploiting Adsorption/Diffusion Synergy in MFI-Catalyzed Hexane Isomerization Reactor

Rajamani Krishna

Van ‘t Hoff Institute for Molecular Sciences

University of Amsterdam

Science Park 904

1098 XH Amsterdam, The Netherlands

email: r.krishna@contact.uva.nl

DOI: 10.1002/cite.202300005

ORCID 0000-0002-4784-8530

Contents

1 The Maxwell-Stefan Diffusion Formulation

Within micro-porous crystalline materials, such as zeolites, and metal-organic frameworks (MOFs), the guest molecules exist in the adsorbed phase. The Maxwell-Stefan (M-S) eqs for *n*-component diffusion in porous materials is applied in the following manner[1-3]

$$
\begin{aligned}
-\frac{\partial \mu_1}{\partial r} &= \frac{RT}{Đ_{12}} x_2 \left(u_1 - u_2\right) + \frac{RT}{Đ_{13}} x_3 \left(u_1 - u_3\right) + \ldots + \frac{RT}{Đ_1}\left(u_1\right) \\
-\frac{\partial \mu_2}{\partial r} &= \frac{RT}{Đ_{21}} x_1 \left(u_2 - u_1\right) + \frac{RT}{Đ_{23}} x_3 \left(u_2 - u_3\right) + \ldots + \frac{RT}{Đ_2}\left(u_2\right) \\
&\cdots\cdots \\
-\frac{\partial \mu_n}{\partial r} &= \frac{RT}{Đ_{n1}} x_1 \left(u_n - u_1\right) + \frac{RT}{Đ_{n2}} x_2 \left(u_n - u_3\right) + \ldots + \frac{RT}{Đ_n}\left(u_n\right)
\end{aligned}
\tag{S1}
$$

The left members of eq (S1) are the negative of the gradients of the chemical potentials, with the units N mol^{-1}; it represents the driving force acting per mole of species 1, 2, 3,..*n*. The u_i represents the velocity of motion of the adsorbate, defined in a reference frame with respect to the framework material. The crystalline framework is considered to be stationary. The term $RT/Đ_i$ is interpreted as the drag or friction coefficient between the guest species *i* and the pore wall. The term $RT/Đ_{ij}$ is interpreted as the friction coefficient for the *i-j* pair of guest molecules. The multiplier $x_i = q_i / q_t$ where q_i is the molar loading of adsorbate, and q_t is the *total* mixture loading $q_t = \sum_{i=1}^{n} q_i$. We expect the friction to be dependent on the number of molecules of *j* relative to that of component *i*.

An important, persuasive, argument for the use of the M-S formulation for mixture diffusion is that the M-S diffusivity $Đ_i$ in mixtures can be estimated using information on the loading dependence of the corresponding unary diffusivity values. Put another way, the M-S diffusivity . $Đ_i$. can be estimated from experimental data on *unary* diffusion in the porous material.

The M-S diffusivity $Đ_{ij}$ has the units m^2 s^{-1} and the physical significance of an *inverse* drag coefficient. The magnitudes of the M-S diffusivities $Đ_{ij}$ do not depend on the choice of the mixture reference velocity because eq (S1) is set up in terms of velocity differences. At the molecular level, the $Đ_{ij}$ reflect how the facility for transport of species *i correlates* with that of species *j*; they are also termed *exchange coefficients*.

The Maxwell-Stefan diffusion formulation (S1) is consistent with the theory of irreversible thermodynamics. The Onsager Reciprocal Relations imply that the M-S pair diffusivities are symmetric

$$Đ_{ij} = Đ_{ji} \tag{S2}$$

We define N_i as the number of moles of species *i* transported per m^2 of crystalline material per second

$$N_i \equiv \rho q_i u_i \tag{S3}$$

where . ρ . is the framework density with units of kg m^{-3}. Multiplying both sides of eq (S1) by ρq_i, the M-S equations for *n*-component diffusion in zeolites, MOFs, and ZIFs take the form [1, 4, 5]

$$-\rho \frac{q_i}{RT}\frac{\partial \mu_i}{\partial r} = \sum_{\substack{j=1 \\ j\neq i}}^{n} \frac{x_j N_i - x_i N_j}{Đ_{ij}} + \frac{N_i}{Đ_i}; \qquad i = 1, 2, ..n \tag{S4}$$

The fluxes N_i in eqs (S4) are defined in terms of the moles transported per m^2 of the *total surface of crystalline material*.

Watch also the video presentation titled **Diffusion in Micropores** on YouTube

https://www.youtube.com/@rajamanikrishna250/videos

2 IAST calculations of mixture adsorption equilibrium

2.1 Brief outline of theory

Within microporous crystalline materials such as zeolites and metal-organic frameworks (MOFs), the guest molecules exist in the adsorbed phase. The Gibbs adsorption equation in differential form is

$$Ad\pi = \sum_{i=1}^{n} q_i d\mu_i \tag{S5}$$

The quantity A is the surface area per kg of framework, with units of m^2 per kg of the framework of the crystalline material; q_i is the molar loading of component i in the adsorbed phase with units moles per kg of framework; μ_i is the molar chemical potential of component i. The spreading pressure π has the same units as surface tension, i.e. N m^{-1}.

The chemical potential of any component in the adsorbed phase, μ_i, equals that in the bulk fluid phase. If the partial fugacities in the bulk fluid phase are f_i, we have

$$d\mu_i = RTd\ln f_i \tag{S6}$$

where R is the gas constant (= 8.314 J mol^{-1} K^{-1}).

Briefly, the basic equation of Ideal Adsorbed Solution Theory (IAST) theory of Myers and Prausnitz[6] is the analogue of Raoult's law for vapor-liquid equilibrium, i.e.

$$f_i = P_i^0 x_i; \quad i = 1, 2, ...n \tag{S7}$$

where x_i is the mole fraction in the adsorbed phase

$$x_i = \frac{q_i}{q_1 + q_2 + ...q_n} \tag{S8}$$

and P_i^0 is the pressure for sorption of every component i, which yields the same spreading pressure, π for each of the pure components, as that for the mixture:

$$\frac{\pi A}{RT} = \int_0^{P_1^0} \frac{q_1^0(f)}{f} df = \int_0^{P_2^0} \frac{q_2^0(f)}{f} df = \int_0^{P_3^0} \frac{q_3^0(f)}{f} df = ... \tag{S9}$$

where $q_i^0(f)$ is the *pure* component adsorption isotherm. The units of $\frac{\pi A}{RT} \equiv \Phi$, also called the surface potential,[7, 8] are mol kg^{-1}; the surface potential has also been called the adsorption potential in several recent publications.[9-12]

The unary isotherm may be described by say the 1-site Langmuir isotherm

$$q^0(f) = q_{sat}\frac{bf}{1+bf}; \quad \theta = \frac{bf}{1+bf} \tag{S10}$$

where we define the fractional *occupancy* of the adsorbate molecules, $\theta = q^0(f)/q_{sat}$. The superscript 0 is used to emphasize that $q^0(f)$ relates the *pure component* loading to the bulk fluid fugacity. More generally, the unary isotherms may need to be described by, say, the dual-site Langmuir-Freundlich model

$$q^0(f) = q_{A,sat}\frac{b_A f^{\nu_A}}{1+b_A f^{\nu_A}} + q_{B,sat}\frac{b_B f^{\nu_B}}{1+b_B f^{\nu_B}} \tag{S11}$$

Each of the integrals in Eq (S9) can be evaluated analytically:

$$\begin{aligned}
\Phi &= \int_{f=0}^{P_i^0}\frac{q^0(f)}{f}df = \frac{q_{A,sat}}{\nu_A}\ln\left(1+b_A\left(P_i^0\right)^{\nu_A}\right)+\frac{q_{B,sat}}{\nu_B}\ln\left(1+b_B\left(P_i^0\right)^{\nu_B}\right) \\
\Phi &= \int_{f=0}^{P_i^0}\frac{q^0(f)}{f}df = \frac{q_{A,sat}}{\nu_A}\ln\left(1+b_A\left(\frac{f_i}{x_i}\right)^{\nu_A}\right)+\frac{q_{B,sat}}{\nu_B}\ln\left(1+b_B\left(\frac{f_i}{x_i}\right)^{\nu_B}\right)
\end{aligned} \tag{S12}$$

The right members of eq (S12) is a function of P_i^0. For multicomponent mixture adsorption, each of the equalities on the right side of eq (S9) must be satisfied. These constraints may be solved using a suitable equation solver, to yield the set of values of P_1^0, P_2^0, P_3^0,.. P_n^0, all of which satisfy eq (S9). The corresponding values of the integrals using these as upper limits of integration must yield the same value of the surface potential $\frac{\pi A}{RT} \equiv \Phi$ for each component; this ensures that the obtained solution is the correct one.

The adsorbed phase mole fractions x_i are then determined using eq (S7):

$$x_i = \frac{f_i}{P_i^0}; \quad i = 1, 2, ...n \tag{S13}$$

The applicability of eq (S13) mandates that all of the adsorption sites within the microporous material are equally accessible to each of the guest molecules, implying a homogeneous distribution of guest adsorbates within the pore landscape, with no preferential locations of any guest species. The circumstances in which this mandate is not fulfilled are highlighted in recent works.[10-13]

A further key assumption of the IAST is that the enthalpies and surface areas of the adsorbed molecules do not change upon mixing. If the total mixture loading is q_t, the area covered by the adsorbed mixture is $\frac{A}{q_t}$ with units of m^2 (mole mixture)$^{-1}$. Therefore, the assumption of no surface area change due to mixture adsorption translates as $\frac{A}{q_t} = \frac{Ax_1}{q_1^0\left(P_1^0\right)} + \frac{Ax_2}{q_2^0\left(P_2^0\right)} + \cdots \frac{Ax_n}{q_n^0\left(P_n^0\right)}$; the total mixture loading is $q_t = q_1 + q_2 ... + q_n$ is calculated from

$$\frac{1}{q_t} = \frac{x_1}{q_1^0(P_1^0)} + \frac{x_2}{q_2^0(P_2^0)} + ... + \frac{x_n}{q_n^0(P_n^0)} \tag{S14}$$

in which $q_1^0(P_1^0)$, $q_2^0(P_2^0)$,… $q_n^0(P_n^0)$ are determined from the unary isotherm fits, using the sorption pressures for each component P_1^0, P_2^0, P_3^0,.. P_n^0 that are available from the solutions to eqs (S9), and (S12). The occurrence of molecular clustering and hydrogen bonding should be expected to applicability of eq (S14) because the surface area occupied by a molecular cluster is different from that of each of the un-clustered guest molecules in the adsorbed phase.

The entire set of eqs (S7) to (S14) need to be solved numerically to obtain the loadings, q_i of the individual components in the mixture.

Watch also the presentation titled **The IAST for Mixture Adsorption Equilibrium** on YouTube https://www.youtube.com/@rajamanikrishna250/videos

3 Transient breakthroughs in fixed bed reactors

We first analyze the transient diffusion, and reaction within a spherical microporous catalyst.

Watch also the presentation titled **Transient Breakthrough Simulations** on YouTube https://www.youtube.com/@rajamanikrishna250/videos

3.1 Transient diffusion-reaction in microporous catalyst

For most crystal geometries, representation as an equivalent sphere is an acceptable approximation.[14] Indeed, most researchers report their uptake diffusivities in terms of a model that assumes uptake within a single spherical crystalline particle. The values thus obtained for the diffusivities within a spherical crystal can be translated to other crystal geometries by comparing values at the same characteristic dimension, defined as the ratio of the crystal volume to its external suface area. For a spherical shaped crystal of radius r_c, the ratio of the volume to the external surface area is $\frac{\left(\frac{4}{3}\pi r_c^3\right)}{4\pi r_c^2} = \frac{r_c}{3}$.

The radial distribution of molar loadings, q_i, within a spherical crystallite, of radius r_c, is obtained from a solution of a set of differential equations describing the uptake

$$\rho \frac{\partial q_i(r,t)}{\partial t} = -\frac{1}{r^2}\frac{\partial}{\partial r}\left(r^2 N_i\right) + \rho \nu_i R_{kg} \tag{S15}$$

where ν_i is the reaction stoichiometric coefficient; negative for reactants and positive for products; R_{kg} represents the reaction rate expressed as moles per kg catalyst per second. The intra-crystalline fluxes N_i, in turn, are related to the gradients in the molar loading by eq (S30). For the isomerization of n-hexane $\mathrm{nC6(1)} \rightleftarrows \mathrm{3MP(2)} \rightleftarrows \mathrm{22DMB(3)}$ the Langmuir-Hinshelwood (L-H) reaction rate expressions for the two constituent reversible reactions, expressed as mol (kg catalyst)$^{-1}$ s^{-1} are

$$R_1 = \left(k_{f1}q_1 - k_{b1}q_2\right); \quad R_2 = \left(k_{f2}q_2 - k_{b2}q_3\right) \tag{S16}$$

At time $t = 0$, i.e. the initial conditions, the molar loadings $q_i(r,0)$ at all locations r within the crystal are uniform (zero loadings). For all times $t \geq 0$, the exterior of the crystal is brought into contact with a bulk gas mixture at partial pressures p_{i0} that is maintained constant till the crystal reaches thermodynamic equilibrium with the surrounding gas mixture. At any time t, the component loadings at the surface of the particle $q_i(r_c,t) = q_i^*$ is in equilibrium with the bulk phase gas mixture with partial pressures p_{i0}. In the general case, the component loadings are calculated using the Ideal Adsorbed Solution Theory (IAST) of Myers and Prausnitz.[6] Alternatively, in some cases, the mixed-gas Langmuir eq (S27) may be of sufficient accuracy. An important advantage of the use of the mixed-gas Langmuir model is. that the matrix of the thermodynamic correction factors can be determined explicitly using eq (S28).

At time t, during the transient approach to thermodynamic equilibrium, the spatial-averaged component loading within the crystallites of radius r_c is calculated using

$$\overline{q}_i(t) = \frac{3}{r_c^3}\int_0^{r_c} q_i(r,t)r^2 dr \tag{S17}$$

Summing eq (S17) over all n species in the mixture allows calculation of the *total average* molar loading of the mixture within the crystallite

$$\overline{q}_t(t,z) = \sum_{i=1}^{n} \overline{q}_i(t,z) \tag{S18}$$

For n-component transient uptake, the set of eqs (S30), (S15), and (S17), and (S18) need to be solved numerically using robust computational techniques. Eqs (S15) are first subjected to finite volume discretization. One of two strategies can be adopted: (a) equi-volume discretization, or (b) equi-distant discretization; see Figure S1. The choice of the discretization scheme used is crucially important in obtaining accurate, converged results. The choice of equi-volume slices is needed when the gradients of the loadings are particularly steep nearer to $r = r_c$. For either strategy, about 20 – 150 slices were

employed in the simulations presented in this work, depending on the guest/host combination. Combination of the discretized partial differential equations (S15) along with algebraic equations describing mixture adsorption equilibrium (IAST or mixed-gas Langmuir model), results in a set of differential-algebraic equations (DAEs), which are solved using BESIRK.[15] BESIRK is a sparse matrix solver, based on the semi-implicit Runge-Kutta method originally developed by Michelsen,[16] and extended with the Bulirsch-Stoer extrapolation method.[17] Use of BESIRK improves the numerical solution efficiency in solving the set of DAEs. The evaluation of the sparse Jacobian required in the numerical algorithm is largely based on analytic expressions.[18] Further details of the numerical procedures used in this work, are provided by Krishna and co-workers;[18-21] interested readers are referred to our website that contains the numerical details.[19]

3.2 Simulation methodology for transient breakthrough in fixed bed reactors

We describe below the simulation methodology used to perform transient operations of fixed bed reactors (see schematics in Figure S1, and Figure S2). The reactor simulation methodology is the same as used in our earlier publications.[1, 4, 22-24] For an *n*-component gas mixture in plug flow through a fixed bed reactor maintained under isothermal, isobaric, conditions, the molar concentrations in the gas phase at any position and instant of time are obtained by solving the following set of partial differential equations for each of the species *i* in the gas mixture[4, 18, 19, 25]

$$\frac{\partial c_i(t,z)}{\partial t}+\frac{\partial\left(v(t,z)c_i(t,z)\right)}{\partial z}+\frac{\left(1-\varepsilon\right)}{\varepsilon}\rho\frac{\partial \bar{q}_i(t,z)}{\partial t}=0;\quad i=1,2,...n \tag{S19}$$

In eq (S19), t is the time, z is the distance along the adsorber, ρ is the framework density, ε is the bed voidage, v is the interstitial gas velocity, and $\bar{q}_i(t,z)$ is the *spatially averaged* molar loading within the crystallites of radius r_c, monitored at position z, and at time t. The time $t = 0$, corresponds to the time at which the feed mixture is injected at the inlet to the fixed bed. Prior to injection of the feed, it is assumed that an inert, non-adsorbing, gas flows through the fixed bed.

The term $\frac{\partial \bar{q}_i(t,z)}{\partial t}$ in eq (S19) is determined by solving the set of eqs (S15), (S16), (S17), and (S18).

At any time *t*, and position *z*, the component loadings at the outer surface of the particle $q_i(r_c,t,z)$ is in equilibrium with the bulk phase gas mixture with partial pressures $p_i(t,z)$ in the bulk gas mixture. In the general case, the component loadings $q_i(r_c,t,z)$ are calculated using the Ideal Adsorbed Solution Theory (IAST) of Myers and Prausnitz.[6] Alternatively, in some cases, the mixed-gas Langmuir eq (S27) may be of sufficient accuracy.

If the value of $Đ_i/r_c^2$ is large enough to ensure that intra-crystalline gradients are absent and the entire crystallite particle can be considered to be in thermodynamic equilibrium with the surrounding bulk gas phase at that time *t*, and position *z* of the adsorber

$$\bar{q}_i(t,z) = q_i(t,z) \tag{S20}$$

The *interstitial* gas velocity is related to the *superficial* gas velocity by

$$v = \frac{u}{\varepsilon} \tag{S21}$$

In all of the simulations reported in this article, the entire bed of crystalline particles is considered to be devoid of guest constituents at time $t = 0$, i.e. we have the initial condition

$$t = 0; \quad q_i(0,z) = 0 \tag{S22}$$

At time, $t = 0$, the inlet to the adsorber, $z = 0$, is subjected to a step input of the *n*-component gas mixture and this step input is maintained till the end of the adsorption cycle when steady-state conditions are reached.

$$t \geq 0; \quad p_i(0,t) = p_{i0}; \quad u(0,t) = u_0 \tag{S23}$$

where $u_0 = v_0\varepsilon$ is the superficial gas velocity at the inlet to the adsorber.

Typically, the adsorber length is divided into 100 slices, and each spherical crystallite was discretized into 20 - 150 equi-volume slices. The results thus obtained were confirmed to be of adequate accuracy. Combination of the discretized partial differential equations (PDEs) along with the algebraic equations

describing mixture adsorption equilibrium (IAST, or mixed-gas Langmuir model, as appropriate), results in a set of differential-algebraic equations (DAEs), which are solved using BESIRK.[15] BESIRK is a sparse matrix solver, based on the semi-implicit Runge-Kutta method originally developed by Michelsen,[16] and extended with the Bulirsch-Stoer extrapolation method.[17] Use of BESIRK improves the numerical solution efficiency in solving the set of DAEs. The evaluation of the sparse Jacobian required in the numerical algorithm is largely based on analytic expressions.[18] Further details of the numerical procedures used in this work, are provided by Krishna and co-workers;[18-21] interested readers are referred to our website that contains the numerical details.[19]

For all the simulations reported in this article we choose the following: adsorber length, L = 0.3 m; cross-sectional area, A = 1 m^2; superficial gas velocity in the bed, u_0 = 0.04 m s^{-1}; voidage of the packed bed, ε = 0.4. Also, the total pressure is assumed to be constant along the length of the fixed bed. Please note that since the superficial gas velocity is specified, the specification of the cross-sectional area of the tube, A, is not relevant in the simulation results presented. The total volume of the bed is $V_{bed} = LA$. The volume of zeolite or MOF used in the simulations is $V_{ads} = LA(1-\varepsilon)$ = 0.18 m^3. If ρ is the framework density, the mass of the catalyst in the bed is $m_{cat} = \rho LA(1-\varepsilon)$ kg. It is important to note that the volume of adsorbent, V_{ads} , includes the pore volume of the adsorbent material. In these breakthrough simulations we use the same volume of adsorbent in the breakthrough apparatus, i.e. (1 - ε) A L = 0.18 m^3 = 180 L.

The transient breakthrough data for the molar concentrations at the exit of the fixed bed, c_i , are plotted as a function of a modified time parameter defined by

$$\frac{\left(F_0 = \text{molar flow rate mol s}^{-1}\right)\times\left(\text{time in s}\right)}{\left(\text{kg catalyst packed in reactor}\right)} = \frac{F_0 t}{m_{cat}} = \text{mol kg}^{-1} \qquad \text{(S24)}$$

3.3 List of Figures for Transient breakthroughs in fixed bed reactors

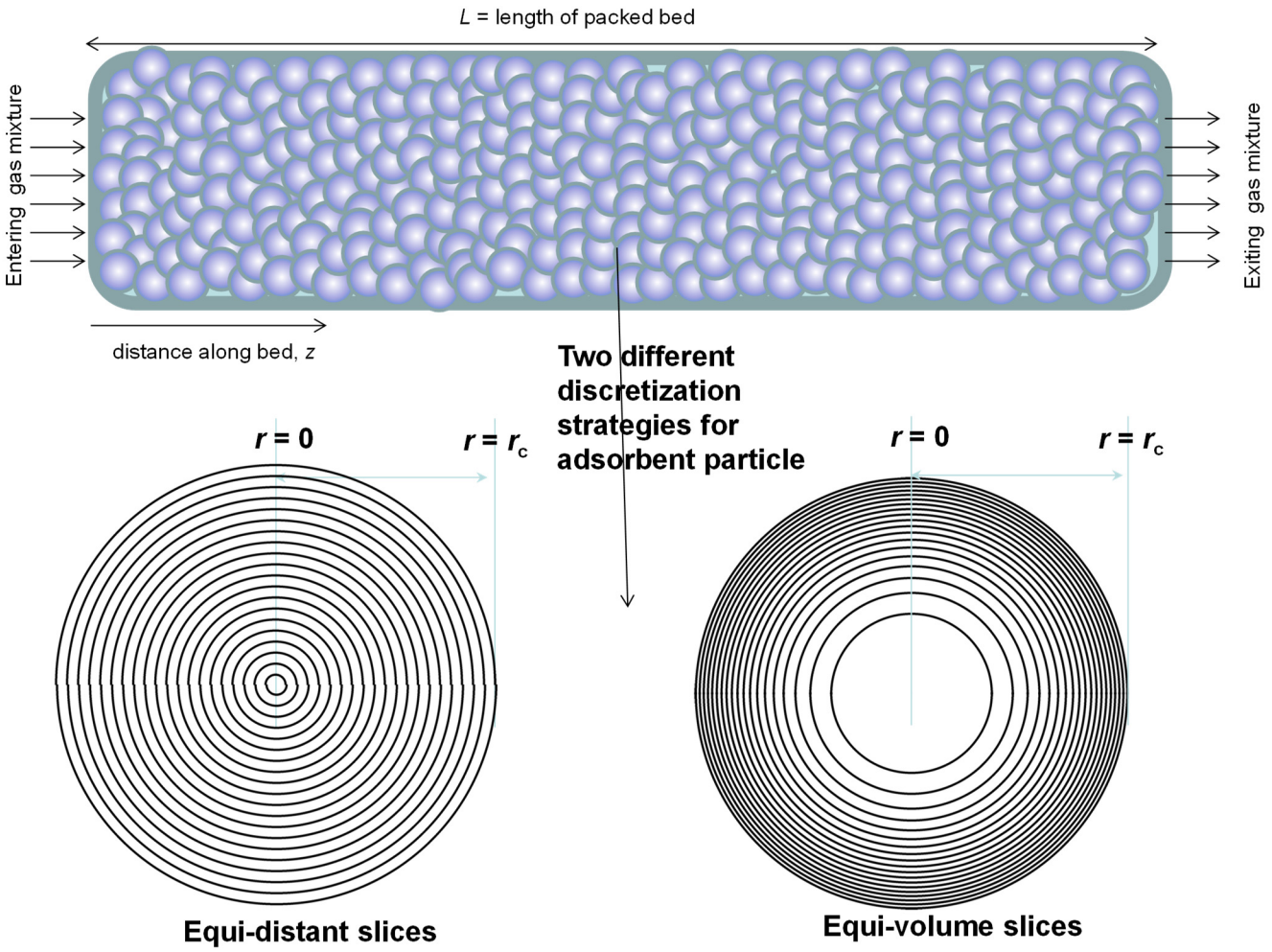

Figure S1. Two different discretization schemes for a single spherical crystallite.

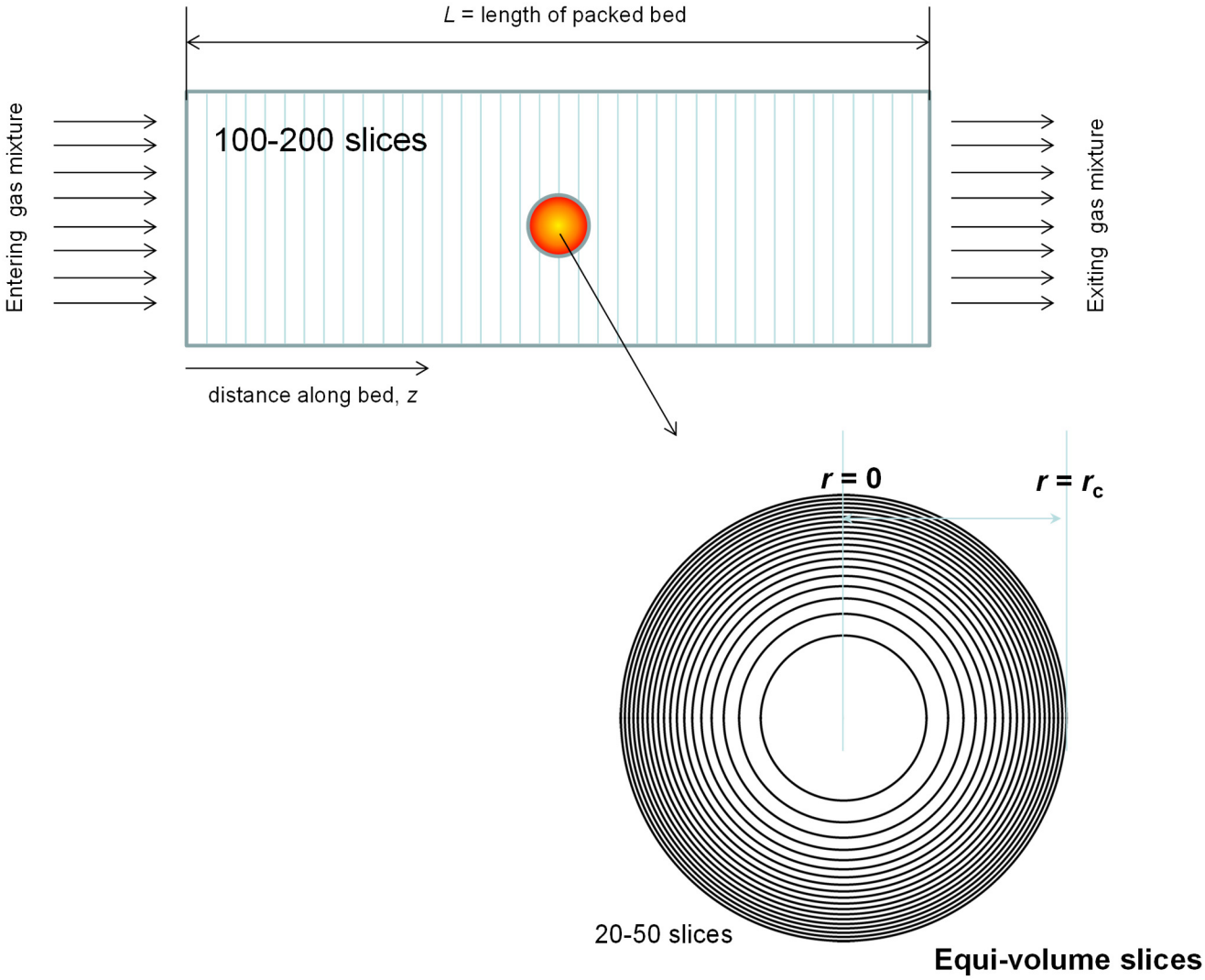

Figure S2. Discretization scheme for fixed bed adsorber.

3.4 Thermodynamic correction factors

At thermodynamic equilibrium, the chemical potential of component *i* in the bulk fluid mixture equals the chemical potential of that component in the adsorbed phase. For the bulk fluid phase mixture we have

$$\frac{1}{RT}\frac{\partial \mu_i}{\partial r} = \frac{\partial \ln f_i}{\partial r} = \frac{1}{f_i}\frac{\partial f_i}{\partial r}; \qquad i = 1, 2, ..n \tag{S25}$$

In eq (S25), f_i represent the partial fugacities in the bulk fluid phase mixture. The chemical potential gradients $\partial \mu_i / \partial r$ can be related to the gradients of the molar loadings, q_i, by defining thermodynamic correction factors Γ_{ij}

$$\frac{q_i}{RT}\frac{\partial \mu_i}{\partial r} = \sum_{j=1}^{n} \Gamma_{ij}\frac{\partial q_j}{\partial r}; \quad \Gamma_{ij} = \frac{q_i}{f_i}\frac{\partial f_i}{\partial q_j}; \qquad i, j = 1, ...n \tag{S26}$$

The thermodynamic correction factors Γ_{ij} can be calculated by differentiation of the model describing mixture adsorption equilibrium. Generally speaking, the Ideal Adsorbed Solution Theory (IAST) of Myers and Prausnitz[6] is the preferred method for estimation of mixture adsorption equilibrium.

In some special case, the mixed-gas Langmuir model

$$\frac{q_i}{q_{i,sat}} = \theta_i = \frac{b_i f_i}{1 + \sum_{i=1}^{n} b_i f_i}; \quad i = 1, 2, ...n \tag{S27}$$

may be of adequate accuracy. Analytic differentiation of eq (S27) yields

$$\Gamma_{ij} = \delta_{ij} + \left(\frac{q_{i,sat}}{q_{j,sat}}\right)\left(\frac{\theta_i}{\theta_V}\right); \qquad i, j = 1, 2 \ldots n \tag{S28}$$

where the fractional vacancy θ_V is defined as

$$\theta_V = 1 - \theta_t = 1 - \sum_{i=1}^{n} \theta_i \tag{S29}$$

The elements of the matrix of thermodynamic factors Γ_{ij} can be calculated explicitly from information on the component loadings q_i in the adsorbed phase; this is the persuasive advantage of the use of the mixed-gas Langmuir model. By contrast, the IAST does not allow the calculation of Γ_{ij} explicitly from knowledge on the component loadings q_i in the adsorbed phase; a numerical procedure is required.

In the scenario in which correlation effects are of negligible importance, eqs (S4) simplify to yield

$$N_i = -\rho Đ_i \sum_{j=1}^{n} \Gamma_{ij} \frac{\partial q_j}{\partial r}; \qquad i = 1, 2..n \tag{S30}$$

Furthermore, if thermodynamic correction factors are also ignored, eq (S4) reduces to a set of uncoupled equations

$$N_i = -\rho Đ_i \frac{\partial q_i}{\partial r}; \qquad i = 1, 2..n \tag{S31}$$

Watch also the video presentation titled **Diffusion in Micropores** on YouTube

https://www.youtube.com/@rajamanikrishna250/videos

4 Deriving Langmuir-Hinshelwood Kinetic Expressions

Within the micropores of zeolite catalysts, the appropriate expression for the reaction kinetics needs to be set up in terms of the component loadings in the adsorbed phase, q_i. Equilibrium thermodynamics tells us that the Gibbs free energy should be at a minimum.[26, 27] The change in the Gibbs free energy is given by eq . For a reacting mixture we obtain

$$dG = -SdT + Ad\pi + \sum \mu_i \nu_i d\chi \tag{S32}$$

where ν_i is the stoichiometric coefficient and χ the fractional conversion. At constant spreading pressure and temperature, eq (S32) simplifies to yield

$$dG = \sum \mu_i \nu_i d\chi \tag{S33}$$

In order to reach a minimum of the Gibbs free energy we have to satisfy the relation

$$\left(\frac{\partial g}{\partial \chi}\right)_{\pi,T} = \sum \nu_i \mu_i = 0 \tag{S34}$$

Substituting the chemical potential in the adsorbed phase

$$\mu_i^{ads}(T,\pi,x_1,...) = g_i^0(T) + RT\ln(P_i^0) + RT\ln(\gamma_i x_i) \tag{S35}$$

results in

$$\begin{aligned} &\sum \nu_i \left(g_i^0(T) + RT\ln(P_i^0) + RT\ln(\gamma_i x_i)\right) = 0 \\ &\exp\left(\sum \nu_i \frac{g_i^0(T)}{RT}\right) = \prod \left(P_i^0 \gamma_i x_i\right)^{\nu_i} \end{aligned} \tag{S36}$$

The left hand side describes the equilibrium constant Therefore, for an ideal adsorbed solution we obtain

$$K_{eq} = \prod \left(P_i^0 x_i \right)^{\nu_i} \tag{S37}$$

At thermodynamic equilibrium we know that the chemical potentials in the gas and adsorbed phase are equal, $\mu^{\text{gas}} = \mu^{\text{ads}}$. Therefore, $P_i^0 x_i = p_i$ applies and therefore

$$K_{eq} = \prod \left(P_i^0 x_i \right)^{\nu_i} = \prod \left(p_i \right)^{\nu_i} \tag{S38}$$

Consider an isomerization reaction: A↔B.

$$K_{eq} = \frac{P_2^0 x_2}{P_1^0 x_1} = \frac{P_2^0 q_2}{P_1^0 q_1} = \frac{p_2}{p_1} \tag{S39}$$

Equation (S39) is general and holds for IAST theory as well as the mixed gas Langmuir model.

Let us assume that the mixed-gas Langmuir model for mixture adsorption equilibrium relates the fractional occupancies, θ_i, molar loadings, q_i, of components 1 (= A_1) and 2 (= A_2) to the partial pressures p_1 and p_2 in the bulk gas phase surrounding the zeolite catalyst:

$$\theta_1 = \frac{q_1}{q_{1,sat}} = \frac{b_1 p_1}{1 + b_1 p_1 + b_2 p_2} = b_1 p_1 \theta_V ; \quad \theta_2 = \frac{q_2}{q_{2,sat}} = \frac{b_2 p_2}{1 + b_1 p_1 + b_2 p_2} = b_2 p_2 \theta_V \tag{S40}$$

The Langmuir-Hinshelwood (L-H) kinetic expression relates the reaction rate to the fractional occupancies θ_i. The expression for the net forward reaction rate, expressed in terms of moles per kg catalyst per second, is

$$\begin{aligned} R_{kg} &= k_1^\theta \theta_1 - k_2^\theta \theta_2 = k_1 q_1 - k_2 q_2 \\ k_1^\theta &\equiv q_{1,sat} k_1 ; \quad k_2^\theta \equiv q_{2,sat} k_2 \end{aligned} \tag{S41}$$

Combination of eqs (S40), and (S41) allows the L-H expression to be expressed in terms of the partial pressures

$$R_{kg} = k_1^{\theta}\theta_1 - k_2^{\theta}\theta_2 = \frac{k_1 q_{1,sat} b_1 p_1 - k_2 q_{2,sat} b_2 p_2}{1 + b_1 p_1 + b_2 p_2} = \left(k_1 q_{1,sat} b_1 p_1 - k_2 q_{2,sat} b_2 p_2\right)\theta_V = \left(k_1^p p_1 - k_2^p p_2\right)\theta_V \quad \text{(S42)}$$

$$k_1^p \equiv k_1 q_{1,sat} b_1; \quad k_2^p \equiv k_2 q_{2,sat} b_2$$

We conclude that the L-H expression is consistent with the mixed-gas Langmuir model for describing mixture adsorption. More generally, we may use the rate expression (S41) wherein the component loadings q_1, and q_2 are determined using the IAST.

In the foregoing, the L-H expression has been expressed in three different, but entirely equivalent, ways; in each case, the reaction rate constants have different units. In eq the reaction rate constants k_1, k_2 have the units: s^{-1}; the reaction rate constants $k_1^{\theta}, k_2^{\theta}$ have the units: mol kg^{-1} s^{-1}. In eq the reaction rate constants k_1^p, k_2^p have the units: mol kg^{-1} Pa^{-1} s^{-1}. In the calculations and simulations presented in this article, we choose the rate expression in terms of the molar loadings, $R_{kg} = k_1 q_1 - k_2 q_2$.

Watch also the video presentation titled **Langmuir-Hinshelwood Kinetics** on YouTube

https://www.youtube.com/@rajamanikrishna250/videos

5 Alkane isomerization reactor

5.1 Background on hexane isomerization process

The Research Octane Numbers (RON) of hexane isomers increase with degree of branching. The RON values are: n-hexane (nC6) = 30, 2-methylpentane (2MP) = 74.5, 3-methylpentane (3MP) = 75.5, 2,2 dimethylbutane (22DMB) = 94, 2,3 dimethylbutane (23DMB) = 105. Therefore, branched isomers are preferred components for incorporation into the high-octane gasoline pool. The isomerization of n-hexane (nC6) to mono-branched and di-branched isomers is an important process in the petroleum industry for octane enhancement of gasoline. Zeolites such as MOR or MFI are commonly used catalysts for hexane isomerization; see process scheme in Figure S3. The products of the isomerization reactor, containing unreacted nC6 along with the branched isomers are separated in a pressure swing adsorption (PSA) scheme. Currently, the separation of hexane isomers is performed using LTA-5A zeolite that operates on the principle of molecular sieving. Linear nC6 can hop from one cage to the adjacent cage through the 4 Å windows of LTA-5A, but branched isomers are largely excluded. The raffinate phase consisting of the branched isomers is incorporated into the gasoline pool. The extract phase from the PSA unit consisting of the linear nC6 is recycled back to the isomerization reactor. An alternative to use of LTA-5A zeolite in the PSA unit is to use MFI zeolite that relies on subtle entropy effects to achieve separations,[28] as described in the following section.

5.2 Configurational-entropy effects in MFI zeolite

MFI zeolite has a topology consisting of a set of intersecting straight channels, and zig-zag (or sinusoidal) channels of approximately 5.5 Å size. The pore landscapes and structural details are provided in Figure S4, and Figure S5. Figure S6 shows the computational snapshots for nC6, 2MP,

3MP, and 22DMB within the intersecting channels of MFI zeolite. The linear nC6 can locate anywhere along the straight and zig-zag channels; the linear isomer is not "configurationally challenged". Mono-branched 2MP, 3MP and di-branched 22DMB prefer to locate at the intersections of MFI, because these are too bulky to locate within the channels; these branched isomers are subject to a configurational "penalty".[28]

Figure S7a shows the unary isotherms of nC6 and 2MP in MFI zeolite at 300 K. Due to configurational considerations, 2MP molecules prefer to locate at the channel intersections because of the extra "leg room" that is available here. There are four intersection sites per unit cell, and therefore the saturation capacity of 2MP is limited to 4 molecules uc^{-1}, for bulk fugacities ranging to 100 Pa..[29-32] The continuous solid lines are dual-site Langmuir-Freundlich fits; the unary isotherm fit parameters are provided in Table S3. Figure S7b presents CBMC simulations of component loadings of binary 50/50 nC6/2MP mixtures in MFI zeolite at 300 K. At bulk fluid phase fugacities higher than 10 Pa, configurational entropy effects lead to almost total exclusion of 2MP.

Figure S8a shows the unary isotherms for nC6, 3MP, and 22DMB at 433 K determined from Configurational-Bias Monte Carlo (CBMC) simulations.[31-33] We note that the saturation capacity of nC6 is 8 molecules per unit cell. The saturation capacities of 3MP and 22DMB are limited to 4 molecules per unit cell. The continuous lines are the fits using the dual-site Langmuir-Freundlich model; the parameter values are specified in Table S1. fitted with the dual-site Langmuir-Freundlich model.

Figure S8b presents CBMC simulations (denoted by symbols), of loadings in MFI zeolite at 433 K for equimolar $\left(f_1 = f_2 = f_3\right)$ ternary nC6(1)/3MP(2)/22DMB(3) mixtures. The continuous solid lines are calculations using IAST, with parameter values specified in Table S1. The IAST predictions are in very good agreement with the CBMC simulation data. We note from Figure S8b that with increasing values of the total bulk fluid phase fugacity $\left(f_t = f_1 + f_2 + f_3\right)$ the mixture adsorption equilibrium becomes increasingly in favor of the linear isomer nC6.

Entropy effects also manifest for 5-component nC6/2MP/3MP/22DMB/23DMB mixtures in MFI zeolite. The pure component isotherms are shown in Figure S9a; the continuous solid lines are the unary isotherm fits with the dual-site Langmuir-Freundlich model. Figure S9b presents CBMC simulations of component loadings in a 5-component nC6/2MP/3MP/22DMB/23DMB mixture at 433 K as a function of the total hydrocarbons fugacity $\left(f_t = f_1 + f_2 + f_3 + f_4 + f_5\right)$. The CBMC data in Figure S9 lead to the conclusion that MFI zeolite could be used in the PSA technology for separation of hexane isomers in the scheme shown in Figure S3.

5.3 Transient nC6/2MP uptake in MFI zeolite

The transient uptake of nC6/2MP mixtures in microporous crystals of MFI zeolite, exposed to an equimolar gas phase mixture at constant total pressure have been reported by Titze et al.[34] Four different experimental runs were conducted.

In Run 1, the initially virgin MFI crystal is exposed to a gas mixture at p_t = 2.6 Pa. For understanding of the transient uptake, Figure S10 presents the CBMC data for mixture adsorption with indication of the range of loadings involved for the pressure step 0 – 2.6 Pa used. Both nC6 and 2MP loadings increase in the IRM experiments till equilibration is reached. The essential features of the transient uptake can be adequately simulated by choosing : $Đ_1/r_c^2$ = 0.016 s^{-1}; $Đ_2/r_c^2$ = 1.6×10^{-4} s^{-1}; both values are assumed to be constant for the loading range encountered in Run 1. The lower diffusivity of the mono-branched isomer 2MP is due to the severe configurational constraints within 5.5 Å sized channels of MFI. The nC6 overshoot is caused by the off-diagonal elements of $[\Gamma]$. If we take $\Gamma_{ij} = \delta_{ij}$, and invoke eq (S31), the nC6 overshoot disappears.[34] The overshoot of nC6 signifies uphill diffusion within the crystals during transient equilibration; this phenomenon is advantageous in the PSA process for separation of hexane isomers, deployed in a process for octane enhancement of gasoline.[4] The total mixture loading at which the maximum in the nC6 uptake occurs is $\Theta_t \approx 4$ molecules uc^{-1}.

Figure S11a summarizes the experimental data for Run 1, Run 2, Run 3 and Run 4. The transient uptake simulations using the eq (S30) are in good agreement with IRM experimental data for transient uptake of nC6/2MP mixtures in all four different experimental campaigns, Runs 1, 2, 3, and 4, with different step changes in the bulk gas pressures; see Figure S11a.

For Run 2, the initial conditions correspond to the final equilibrated loadings of Run 1. In Run 2 the pressure is increased to 4 Pa. The IRM experiments can be adequately simulated by choosing: $Đ_1/r_c^2$ = 0.02 s^{-1}; $Đ_2/r_c^2$ = 2×10^{-4} s^{-1}; both values are assumed to be constant for the loading range encountered in Run 2.

For Run 3, the initial conditions correspond to the final equilibrated loadings of Run 2. In Run 3 the pressure is increased to 12.2 Pa. For the pressure step from 4 Pa to 12.2 Pa, entropy effects significantly impact on 2MP, and cause its exclusion from the MFI crystals as indicated in the CBMC mixture simulation data in see Figure S11b. The exclusion of 2MP due to entropy effects is reflected in the IRM experimental data The IRM experiments can be adequately simulated by choosing: $Đ_1/r_c^2$ = 0.04 s^{-1}; $Đ_2/r_c^2$ = 4×10^{-4} s^{-1}; both values are assumed to be constant for the loading range encountered in Run 4.

For Run 4, the initial conditions correspond to the final equilibrated loadings of Run 3. In Run 4 the pressure is increased to 102 Pa. For the pressure step from 12.2 Pa to 102 Pa, entropy effects also significantly impact on 2MP, and cause its exclusion from the MFI crystals as indicated in the CBMC mixture simulation data in Figure S11b. The exclusion of 2MP due to entropy effects is reflected in the IRM experimental data The IRM experiments can be adequately simulated by choosing: $Đ_1/r_c^2$ = 0.16 s^{-1}; $Đ_2/r_c^2$ = 1.6×10^{-3} s^{-1}; both values are assumed to be constant for the loading range encountered in Run 4.

In Figure S12 the fitted values of the M-S diffusivities $Đ_{nC6}/r_c^2$ and $Đ_{2MP}/r_c^2$ in each individual campaign is plotted as a function of the loading of 2MP. The ratio of the M-S diffusivities of nC6 and 2MP is maintained at 100.

Each of the diffusivities is strongly dependent on the loading of 2MP, increasing by a factor of 10 as we progress from Run 1 to Run 4; the ratio $Đ_1/Đ_2$ has a constant value of 100. Also indicated at the top of Figure S12 are the values of the total mixture loadings Θ_t for each of the four Runs. We note that as we proceed from Run 1 the total mixture loading increases from $\Theta_t = 4.5$/uc in Run 1, to $\Theta_t = 7.54$/uc in Run 4, the 2MP loading decreases from 1.84/uc to 0.14/uc, emphasizing the significant configurational-entropy effects. Concomitantly, we note that the diffusivities of both species, nC6 and 2MP, increase by about an order of magnitude with increased total mixture loading, Θ_t. While there are many practical examples of increased adsorption leading to a lowering of diffusivities,[35, 36] The diffusion of nC6/2MP mixture in MFI has very special and unusual characteristics; nC6 is much more mobile, by about one order of magnitude. Furthermore, as a consequence of configurational entropy effects, the more strongly adsorbed species is also nC6. We therefore have a mixture of more-mobile-more-strongly-adsorbed-nC6 and tardier-less-strongly-adsorbed-2MP. Configurational entropy effects cause 2MP to be excluded from the adsorbed phase for operations at $\Theta_t > 4$; concomitant with this exclusion is an increase, by about an order of magnitude, in the diffusivities of both species. The nC6/2MP uptake data are unique because the diffusivity trends in Figure S12 imply that there is synergy between mixture adsorption and mixture diffusion; this synergy aspect is discussed in detail by Titze et al.[34]

5.4 Intra-crystalline diffusivities in MFI zeolite

Schuring et al.[37] have reported experimental data on the self-diffusivities of both nC6 and 2MP in nC6/2MP mixtures. These measurements were made at a total loading that is kept nearly constant at 3.5 molecules per unit cell. Their data, that were measured at 433 K shows that *both* self-diffusivities are reduced with increasing loading of 2MP in the mixture; see Figure S13a. The preferential location of

2MP at the intersections causes blocking of molecular traffic in the intersecting channel system of MFI. MD simulations show that such intersection blocking effects also manifest in nC6/22DMB mixtures.[38] We also note that the linear nC6 has a diffusivity that is about an order of magnitude higher than that of the branched 2MP. MD simulations show that the results such as that in Figure S13a also hold for nC6/22DMB mixtures.[38]

We now try to get an estimate of the relative values of diffusivities of the branched isomers in MFI. On the basis of the experimental data on diffusivities of hexane isomers reported by Cavalcante and Ruthven[39] and Jolimaître et al,[40] we note that the hierarchy of diffusivities is 2MP ≈ 3MP > > 23DMB > 22DMB; see Arrhenius plots in Figure S13b,c.

5.5 Simulation of transient uptake in MFI catalyst

Consider uptake within MFI catalyst carrying out the isomerization of nC6 to produce a product containing mono-branched 3-methylpentane (3MP) and di-branched 22DMB. We restrict our analysis to the simplified reaction scheme $\text{nC6(1)} \rightleftarrows \text{3MP(2)} \rightleftarrows \text{22DMB(3)}$ where the Langmuir-Hinshelwood (L-H) reaction rate expressions for the two constituent reversible reactions, expressed as mol (kg catalyst)$^{-1}$ s^{-1} are $R_{kg,1} = \left(k_{f1}q_1 - k_{b1}q_2\right)$; $R_{kg,2} = \left(k_{f2}q_2 - k_{b2}q_3\right)$. The subscripts f and b refer to the forward and reverse reactions, and the subscripts 1 and 2 refer to the first and second isomerization reaction steps. Using our earlier publication as guidelines,[41] we take $k_{f1} = k_{f2} = 0.01$ s^{-1} and $k_{b1} = k_{b2} = 0.004$ s^{-1}. The catalyst radius is taken to be $r_c = 1$ mm.

Figure S14 presents simulations of transient uptake inside MFI catalyst exposed to a gas phase nC6(1)/3MP(2)/22DMB(3) mixture at 433 K. The partial pressures of the components in the bulk gas phase are p_1 =16 kPa; p_2 = 0.2 kPa, p_3 = 0.2 kPa. The mixture adsorption equilibrium is determined using the IAST. The M-S diffusivities are chosen as $Đ_1/r_c^2 = 2\times10^{-4}$ s^{-1}; $Đ_2/r_c^2 = 2\times10^{-5}$ s^{-1}; $Đ_3/r_c^2 = 1\times10^{-5}$ s^{-1}; the choice of these diffusivities is based on the experimental data presented in Figure S13.[1, 4,

[34, 42] The continuous solid lines represent uptake simulations with the flux equations (S30). We note that the most mobile nC6 displays an overshoot during transient uptake; this signifies uphill diffusion.[1, 43, 44]

Figure S15 shows the corresponding transient uptakes for the reversible isomerization reaction $2MP(1) \rightleftarrows 22DMB(2)$ using extrudates of MFI zeolite as catalyst, transient overshoots are observed for 2MP. The rate of chemical reaction, expressed as moles per kg of catalyst per second is written as $R_{kg} = k_f q_1 - k_b q_2$. The reaction rate constants, taken from Baur and Krishna,[45] are k_f = 0.0011 s^{-1}, k_b = 0.00055 s^{-1}. In this case 2MP exhibits a pronounced overshoot in its approach to equilibrium.

5.6 Simulation of fixed bed isomerization reactor

We carried out simulations of a fixed bed reactor packed with MFI catalyst carrying out the $nC6(1) \rightleftarrows 3MP(2) \rightleftarrows 22DMB(3)$ reaction. The reactor operates isothermally at 433 K. The partial pressures of the components in the bulk gas phase at the reactor inlet are p_1 =16 kPa; p_2 = 0.2 kPa, p_3 = 0.2 kPa. The total molar rate of the gas mixture at the reactor inlet is F_0 = 656 mol h^{-1}.

Figure S16a shows the gas phase molar concentration along the length of the fixed bed reactor, plotted as a function of the parameter m_{cat}/F_0, that is linearly related to the length of the fixed bed. At the value of $m_{cat}/F_0 = 0.48$ kg mol^{-1} h, the gas phase concentration of 22DMB exiting the fixed bed ≈ 2 mol m^{-3}.

Figure S16b presents the simulations of the fixed bed reactor for the scenario in which intra-crystalline diffusional influences are considered to be of negligible importance, i.e. $Đ_i/r_c^2 >> 1$; this is achieved by choosing a significantly smaller crystallite size for the catalyst. In this scenario, the gas phase concentration of 22DMB exiting the fixed bed ≈ 2 mol m^{-3} is achieved at the value $m_{cat}/F_0 = 0.08$ kg mol^{-1} h. This implies that the effectiveness of the catalyst is reduced by a factor six due to the strong intra-crystalline diffusional limitations requiring the use of six times the amount of catalyst necessary when diffusion is of negligible importance.

The synergy between mixture adsorption and intra-crystalline diffusion favoring nC6 over 3MP, and in turn 3MP over 22DMB can best be exploited by operating the fixed bed reactor in a transient manner. To illustrate this, Figure S16c presents the simulations of transient reactor operations. The molar concentrations of nC6, 3MP, and 22DMB are plotted as a function of the modified time parameter $F_0 t/m_{cat}$. The component to elute first is 22DMB that has the poorest adsorption strength and the lowest intra-crystalline mobility. The component to elute next is 3MP, and the linear nC6 that has the strongest adsorption strength is the last component to elute the reactor. We note that for values of $F_0 t/m_{cat} < 0.6$ mol kg^{-1}, the exit gas mixture contains predominantly 22DMB and 3MP, the desired products for incorporation into the gasoline. Transient operations of the fixed bed isomerization reactor obviate the need for a subsequent PSA separation unit.

If diffusional limitations are absent, i.e. $Đ_i/r_c^2 >> 1$, achieved by choosing a significantly smaller crystallite size for the catalyst, the three isomers nC6, 3MP and 22DMB exit the reactor at the same time; see Figure S16d. In this scenario, the reactor needs to be followed by a PSA separation step as pictured in Figure S3.

Figure S17 shows the corresponding simulations of a fixed bed reactor packed with MFI catalyst carrying out the $2\text{MP}(1) \rightleftarrows 22\text{DMB}(2)$ reaction, operating isothermally at 473 K. The partial pressures of the components in the bulk gas phase at the reactor inlet are p_1 =40 kPa; p_2 = 1 Pa. The total molar rate of the gas mixture at the reactor inlet is F_0 = 73.2 mol h^{-1} .

Figure S17a shows the gas phase molar concentration along the length of the fixed bed reactor, plotted as a function of the parameter m_{cat}/F_0 , that is linearly related to the length of the fixed bed. At the value of $m_{cat}/F_0 = 1.5$ kg mol^{-1} h , the gas phase concentration of 22DMB exiting the fixed bed ≈ 7.6 mol m^{-3}.

Figure S17b presents the simulations of the fixed bed reactor for the scenario in which intra-crystalline diffusional influences are considered to be of negligible importance, i.e. $Đ_i/r_c^2 >> 1$; this is

achieved by choosing a significantly smaller crystallite size for the catalyst. In this scenario, the gas phase concentration of 22DMB exiting the fixed bed ≈ 7.6 mol m^{-3} is achieved at the value $m_{cat}/F_0 = 0.9$ kg mol^{-1} h . This implies that the effectiveness of the catalyst is reduced by a factor 1.7 due to the strong intra-crystalline diffusional limitations requiring the use of 1.7 times the amount of catalyst necessary when diffusion is of negligible importance.

The synergy between mixture adsorption and intra-crystalline diffusion favoring 2MP over 22DMB, can best be exploited by operating the fixed bed reactor in a transient manner. To illustrate this, Figure S17c presents the simulations of transient reactor operations. The molar concentrations of 2MP, and 22DMB are plotted as a function of the modified time parameter $F_0 t/m_{cat}$. The component to elute first is 22DMB that has the poorest adsorption strength and the lower intra-crystalline mobility. The component to elute next is 2MP. We note that for values of $F_0 t/m_{cat}$ < 0.5 mol kg^{-1}, the exit gas mixture contains predominantly 22DMB, the desired product for incorporation into the gasoline. Transient operations of the fixed bed isomerization reactor obviate the need for a subsequent PSA separation unit.

If diffusional limitations are absent, i.e. $Đ_i/r_c^2 >> 1$, achieved by choosing a significantly smaller crystallite size for the catalyst, the two isomers 2MP and 22DMB exit the reactor at the same time; see Figure S17d.

Animations showing the movement of concentration fronts of the three isomers along the length of the fixed bed reactor are included in my presentation titled **Exploiting Adsorption-Diffusion Synergy in Fixed Bed Catalytic Reactors** on my YouTube channel

https://www.youtube.com/@rajamanikrishna250/videos

5.7 List of Tables for Alkane isomerization reactor

Table S1. Dual-site Langmuir-Freundlich parameters for unary hexane isomers at 433 K in MFI zeolite. $\Theta = \Theta_{A,sat}\frac{b_A p^{\nu_A}}{1+b_A p^{\nu_A}} + \Theta_{i,B,sat}\frac{b_B p^{\nu_B}}{1+b_B p^{\nu_B}}$. The fits are based on CBMC simulation data of Krishna and van Baten.[46]

	Site A			Site B		
	$\frac{\Theta_{A,sat}}{\text{molecules uc}^{-1}}$	$\frac{b_A}{\text{Pa}^{-\nu_A}}$	ν_A	$\frac{\Theta_{B,sat}}{\text{molecules uc}^{-1}}$	$\frac{b_B}{\text{Pa}^{-\nu_B}}$	ν_B
nC6	3.2	2.21×10^{-8}	1.6	4.3	7.42×10^{-4}	1
2MP	4	7.85×10^{-4}	1.03			
3MP	4	4.22×10^{-4}	1.02	1	9.88×10^{-7}	1
22DMB	4	2.55×10^{-4}	1.02			
23DMB	4	4.59×10^{-4}	1.02			

Intra-crystalline diffusion effects are taken into account using the input values as in previous work:[4] $Đ_{nC6}/r_c^2$ = 0.0002 s^{-1}; $Đ_{n\%}/Đ_{3MP}$ =10; $Đ_{nC6}/Đ_{22DMB}$ =40. The Langmuir-Hinshelwood (L-H) reaction rate expressions for the two constituent reversible reactions, expressed as mol (kg catalyst)$^{-1}$ s^{-1} are $R_{kg,1} = \left(k_{f1}q_1 - k_{b1}q_2\right)$; $R_{kg,2} = \left(k_{f2}q_2 - k_{b2}q_3\right)$. The reaction rate constants are k_{f1} = 0.01 s^{-1}, k_{b1} = 0.005 s^{-1}; k_{f2} = 0.01 s^{-1}, k_{b2} = 0.005 s^{-1}. The transient breakthrough simulations are based on eq (S30) taking due account of thermodynamic coupling effects.[3, 47]

Table S2. 1-site Langmuir parameters for unary hexane isomers at 473 K in MFI zeolite. $\Theta = \Theta_{sat} \frac{bp}{1+bp}$.

	$\frac{\Theta_{A,sat}}{\text{molecules uc}^{-1}}$	$\frac{b}{\text{Pa}^{-1}}$
2MP	4	1.27×10^{-4}
22DMB	4	7.118×10^{-5}

Intra-crystalline diffusion effects are taken into account using the input values as in previous work:[4] $Đ_{2MP}/r_c^2$ = 0.005 s^{-1}; 0; $Đ_{2MP}/Đ_{22DMB}$ =80. The Langmuir-Hinshelwood (L-H) reaction rate expression, expressed as mol (kg catalyst)$^{-1}$ s^{-1} are $R_{kg} = \left(k_f q_1 - k_b q_2\right)$. The reaction rate constants, taken from Baur and Krishna,[45] are k_1 = 0.0011 s^{-1}, k_{b1} = 0.00085 s^{-1}; The transient breakthrough simulations are based on eq (S30) taking due account of thermodynamic coupling effects.[3, 47]

Table S3. Dual-site Langmuir-Freundlich parameters for pure component isotherms for hexane isomers in MFI at 300 K. This data is from the Supporting Information of Titze et al.[34] The unary isotherm data are fitted with the dual-Langmuir-Freundlich model

$$\Theta = \Theta_{A,sat}\frac{b_A p^{\nu_A}}{1+b_A p^{\nu_A}} + \Theta_{i,B,sat}\frac{b_B p^{\nu_B}}{1+b_B p^{\nu_B}}$$

	Site A			Site B		
	$\frac{\Theta_{A,sat}}{\text{molecules uc}^{-1}}$.	$\frac{b_A}{\text{Pa}^{-\nu_A}}$	ν_A	$\frac{\Theta_{B,sat}}{\text{molecules uc}^{-1}}$	$\frac{b_B}{\text{Pa}^{-\nu_B}}$	ν_B
nC6	6.6	0.7084	0.83	1.4	16.5765	1.5
2MP	4	4.51	1.05	4	7.92×10^{-6}	1.13

5.8 List of Figures for Alkane isomerization reactor

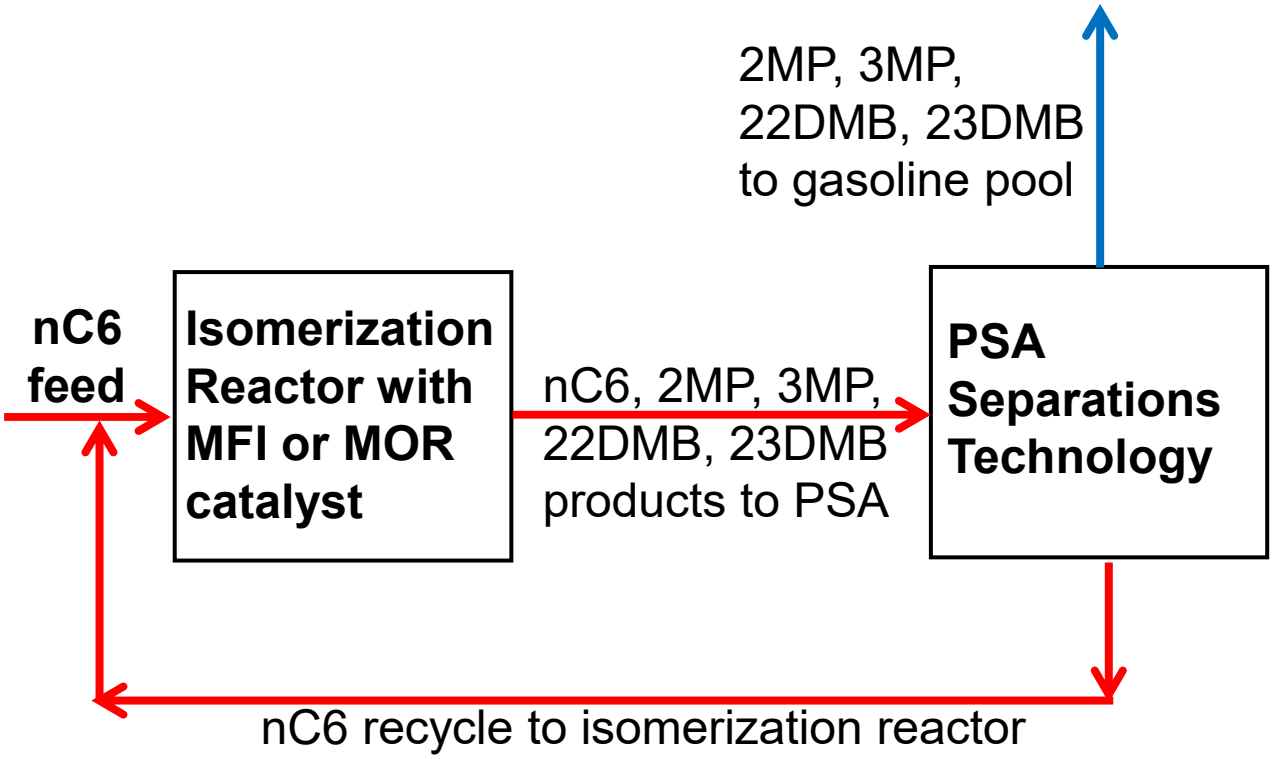

Figure S3. Currently employed processing scheme for nC6 isomerization and subsequent PSA separation step.

	MFI
a /Å	20.022
b /Å	19.899
c /Å	13.383
Cell volume / Å^3	5332.025
conversion factor for [molec/uc] to [mol per kg Framework]	0.1734
conversion factor for [molec/uc] to [kmol/m^3]	1.0477
ρ [kg/m3]	1796.386
MW unit cell [g/mol(framework)]	5768.141
ϕ, fractional pore volume	0.297
open space / Å^3/uc	1584.9
Pore volume / cm^3/g	0.165
Surface area /m^2/g	487.0
DeLaunay diameter /Å	5.16

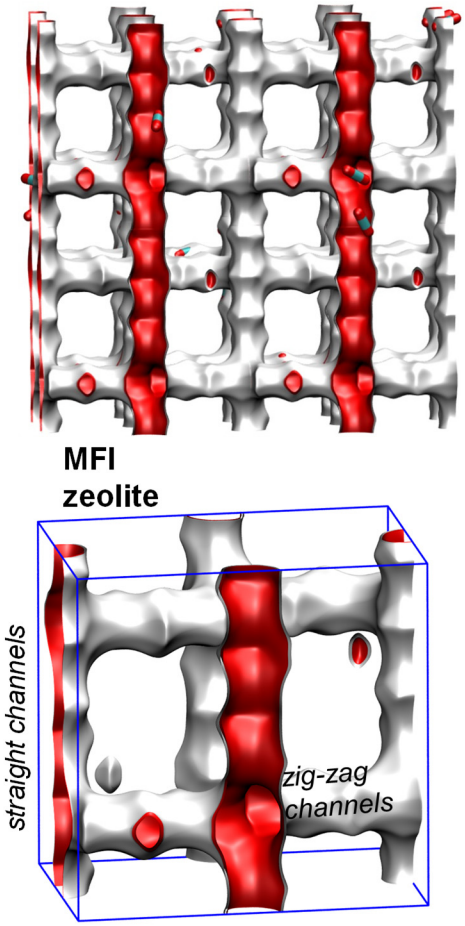

Figure S4. Structural details and pore landscape for MFI zeolite.

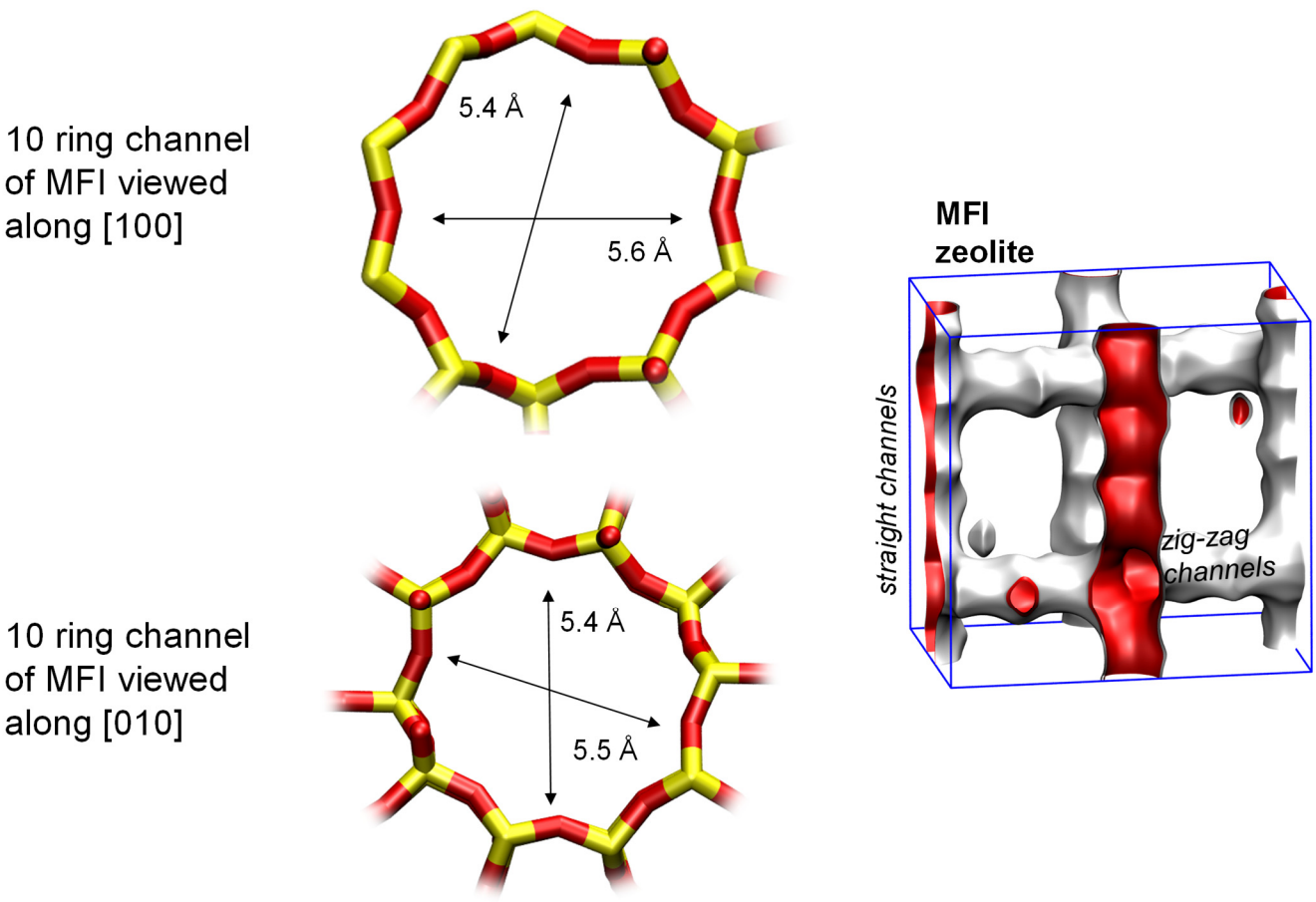

Figure S5. Structural details and pore landscape for MFI zeolite.

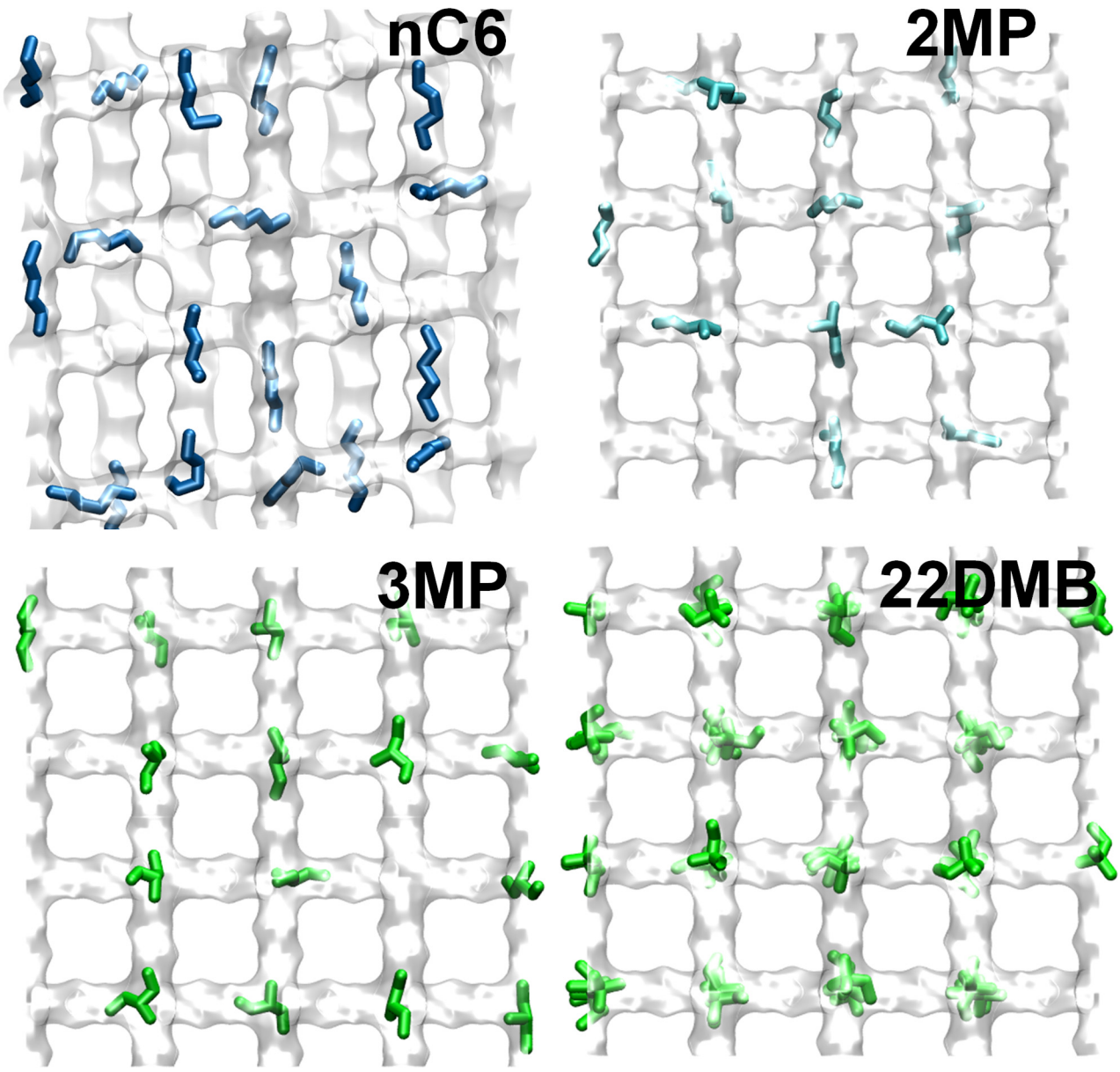

Figure S6. Computational snapshots showing the location of nC6, 2MP, 3MP, and 22DMB within the intersecting channel topology of MFI zeolite.

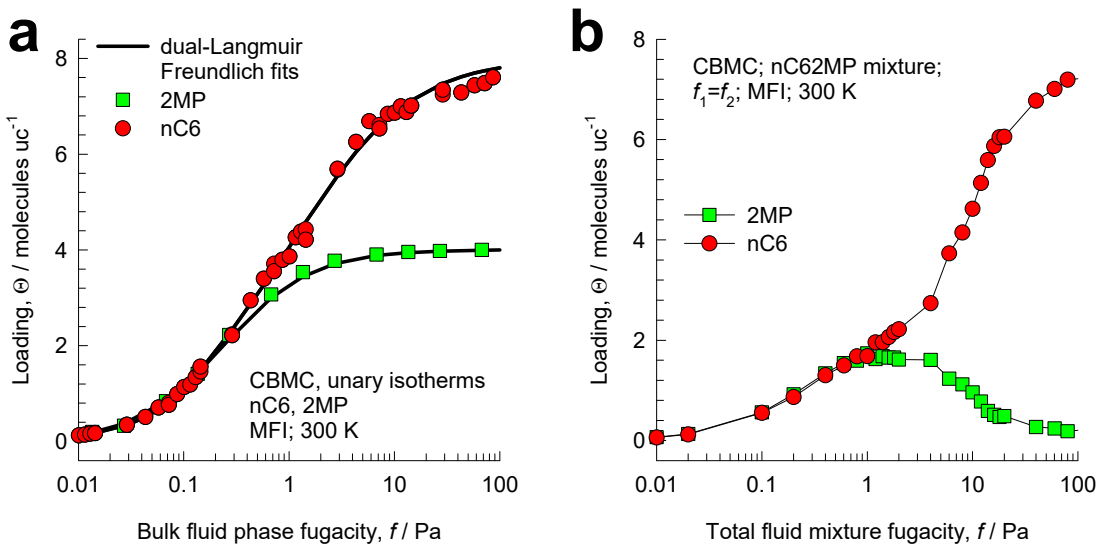

Figure S7. (a) CBMC simulations[34] of unary isotherms of nC6 and 2MP in MFI zeolite at 300 K. The continuous solid lines are dual-site Langmuir-Freundlich fits; the unary isotherm fit parameters are provided in Table S3. (b) CBMC simulations[34] of component loadings of binary 50/50 nC6/2MP mixtures in MFI zeolite at 300 K,

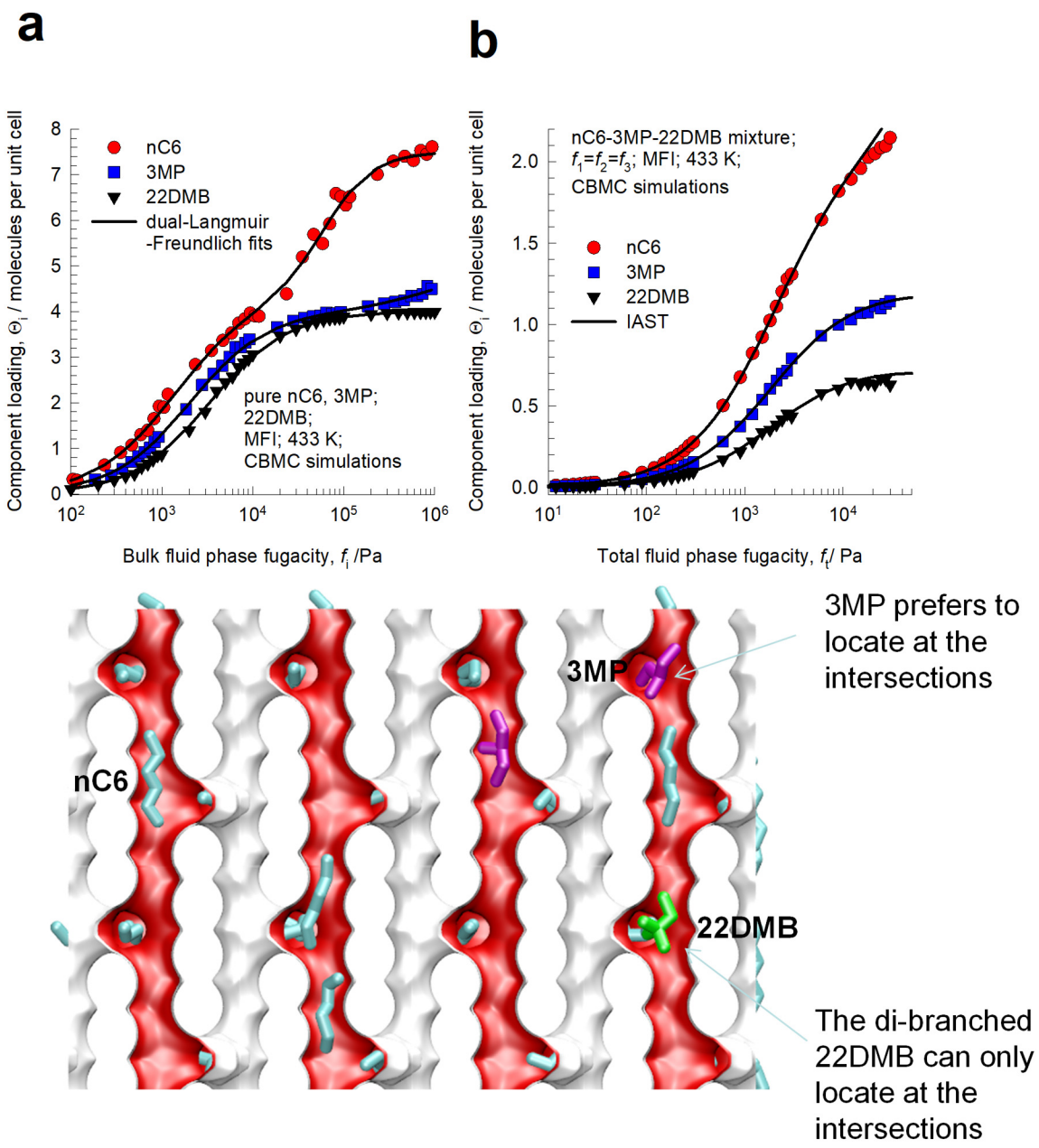

Figure S8. (a) Unary isotherms for nC6, 3MP and 22DMB in MFI at 433 K. The symbols represent CBMC simulation data.[31-33] The continuous lines are the fits using the dual-site Langmuir-Freundlich model; the parameter values are specified in Table S1. (b) CBMC simulations (denoted by symbols), of loadings in MFI zeolite at 433 K for equimolar ternary nC6/3MP/22DMB mixture. The continuous solid lines are calculations using IAST, with parameter values specified in Table S1.

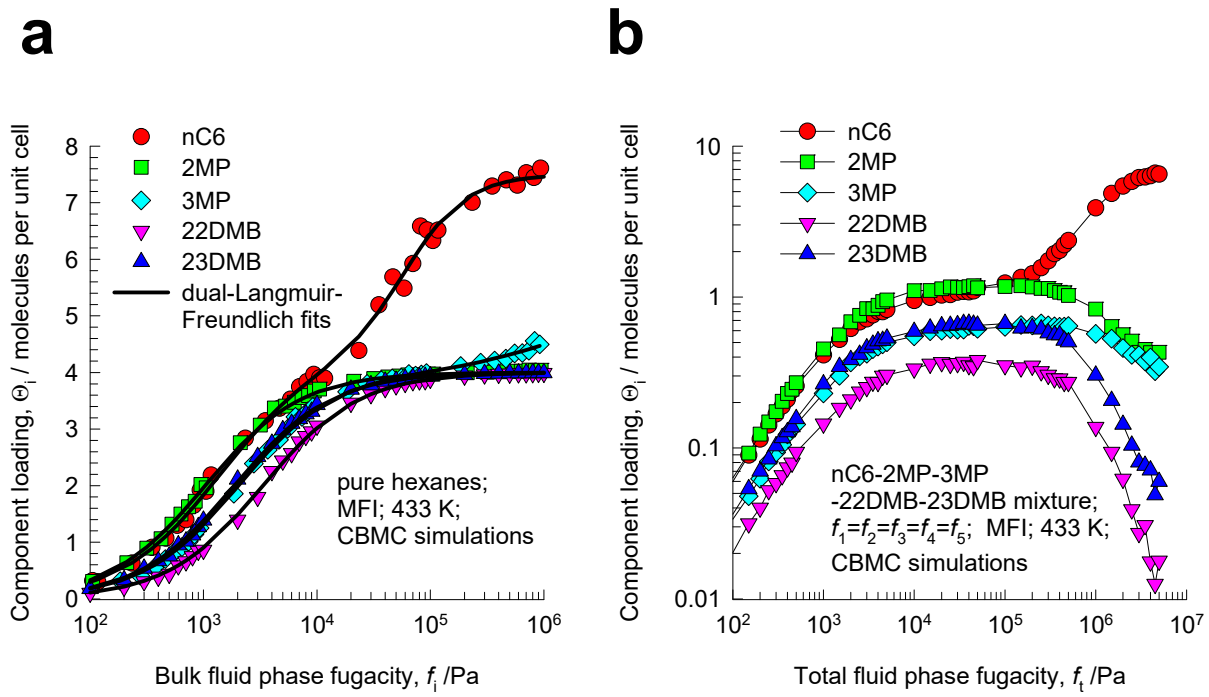

Figure S9. (a) Pure component sorption isotherms for nC6, 2MP, 3MP, 22DMB and 23DMB in MFI at 433 K. The symbols represent CBMC simulation data.[31-33] The continuous lines are the fits using the dual-site Langmuir-Freundlich model; the parameter values are specified in Table S1. (b) CBMC simulations (denoted by symbols), of loadings in MFI zeolite at 433 K for equimolar 5-component nC6/2MP/3MP/22DMB/23DMB mixture.

IR Microscopy

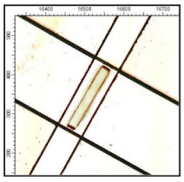

Coffin shaped crystals

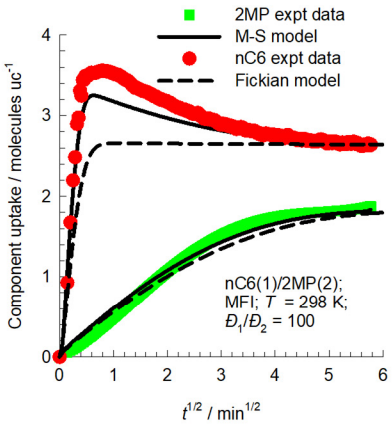

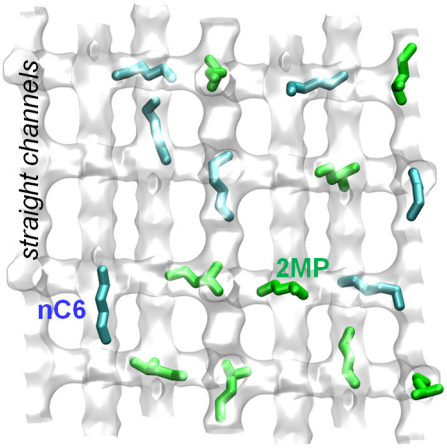

Figure S10. Experimental data of Titze et al.[34] for Run 1 transient uptake of nC6/2MP mixtures in MFI zeolite. Input data simulation of Run 1: $Đ_1/r_c^2$ = 0.016 s^{-1}; $Đ_2/r_c^2$ = 1.6×10^{-4} s^{-1}; $t = 0$; $p_1(r_c,0) = p_2(r_c,0)$ = 0 Pa; $t \geq 0$; $p_1(r_c,t) = p_2(r_c,t)$ = 1.3 Pa. The isotherm data are provided in Table S3.

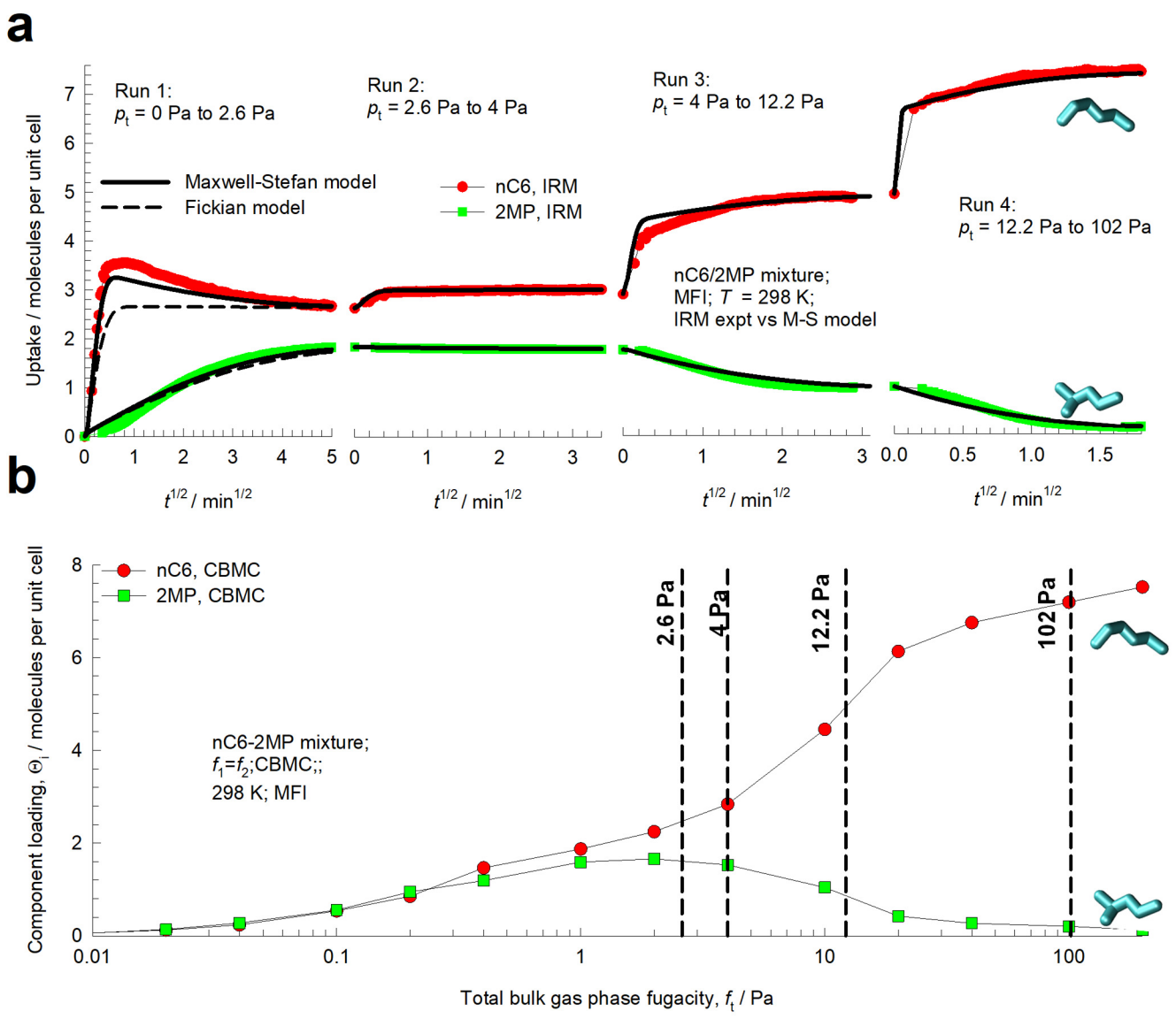

Figure S11. (a) Experimental data of Titze et al.[34] for four different experimental campaigns (Runs 1, 2, 3, and 4) for transient uptake of nC6/2MP mixtures in MFI zeolite with different step changes in the bulk gas pressures. The isotherm data are provided in Table S3. (b) CBMC simulations[34] of component loadings of binary 50/50 nC6/2MP mixtures in MFI zeolite at 300 K,

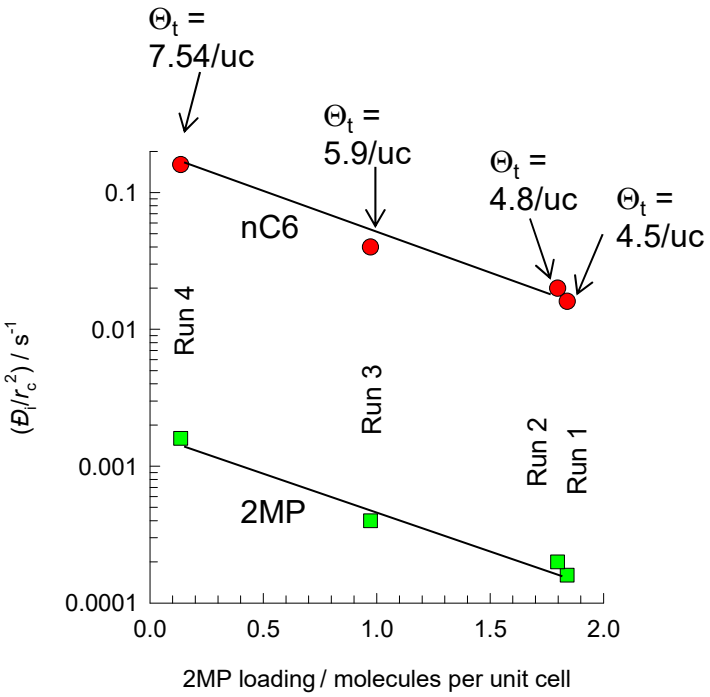

Figure S12. The fitted values of the M-S diffusivities $Đ_{nC6}/r_c^2$ and $Đ_{2MP}/r_c^2$ in each individual campaign is plotted as a function of the loading of 2MP. The ratio of the M-S diffusivities of nC6 and 2MP is maintained at 100.

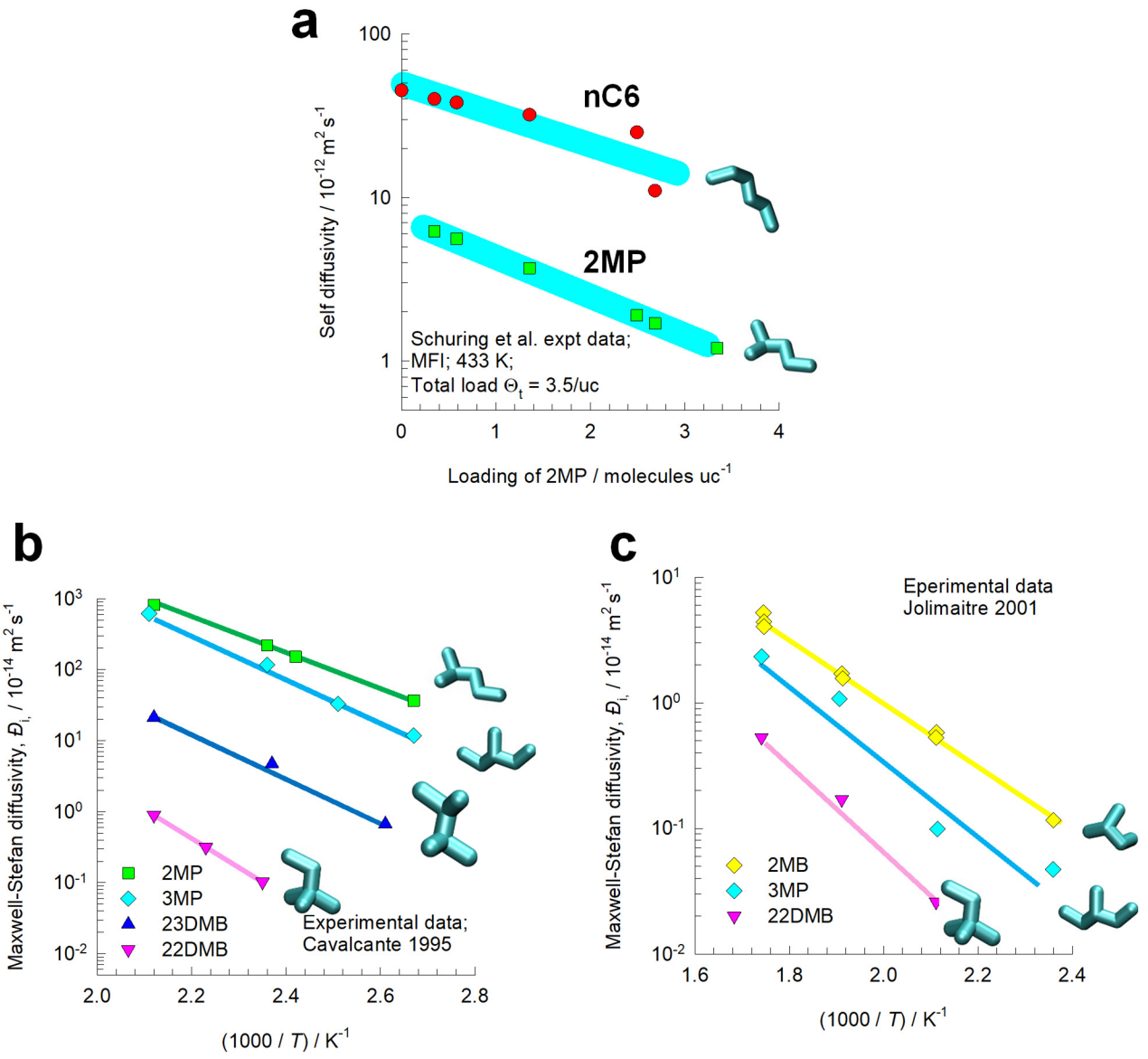

Figure S13. (a) Experimental data[37] on self-diffusivities of nC6 and 2-methylpentane (2MP) as a function of the loading of 2MP, keeping the total loading Θ_t = 3.5 uc^{-1}. (b, c) Arrhenius plot of diffusivities of 2MB, 2MP, 3MP, 22DMB, and 23DMB in MFI zeolite. The data are re-plotted from the experimental results of (b) Cavalcante and Ruthven,[39] and (c) Jolimaître et al.[40]

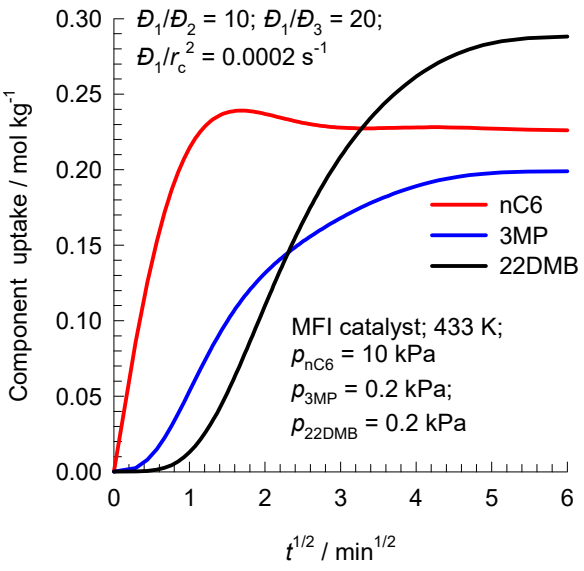

Figure S14. Transient uptake inside MFI catalyst exposed to a gas phase nC6(1)/3MP(2)/22DMB(3) mixture at 433 K, carrying out the isomerization reaction $\text{nC6(1)} \rightleftarrows \text{3MP(2)} \rightleftarrows \text{22DMB(3)}$. The partial pressures of the components in the bulk gas phase are p_1 = 10 kPa; p_2 = 0.2 kPa, p_3 = 0.2 kPa. The input data for isotherms, diffusivities, and reaction rate constants are provided in Table S1. The continuous solid lines represent uptake simulations include thermodynamic coupling using flux eqs (S30).

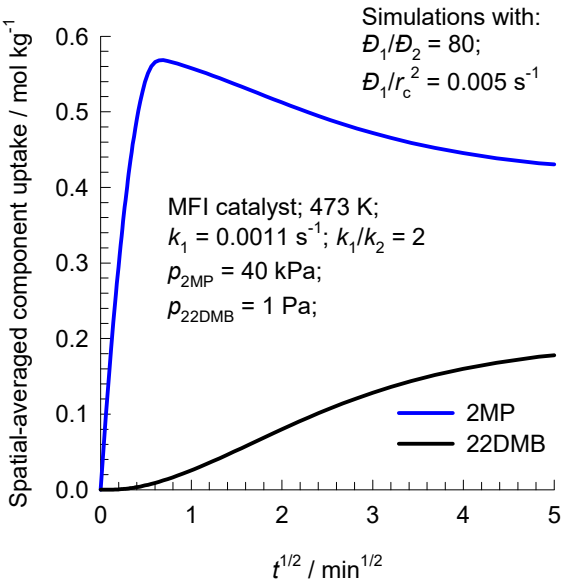

Figure S15. Transient uptake inside MFI catalyst exposed to a gas phase 2MP(1)/22DMB(2) mixture at 473 K, carrying out the isomerization reaction $2\text{MP}(1) \rightleftarrows 22\text{DMB}(2)$. The partial pressures of the components in the bulk gas phase are p_1 = 40 kPa; p_2 = 1 Pa. The input data for isotherms, diffusivities, and reaction rate constants are provided in Table S2. The continuous solid lines represent uptake simulations include thermodynamic coupling using flux eqs (S30).

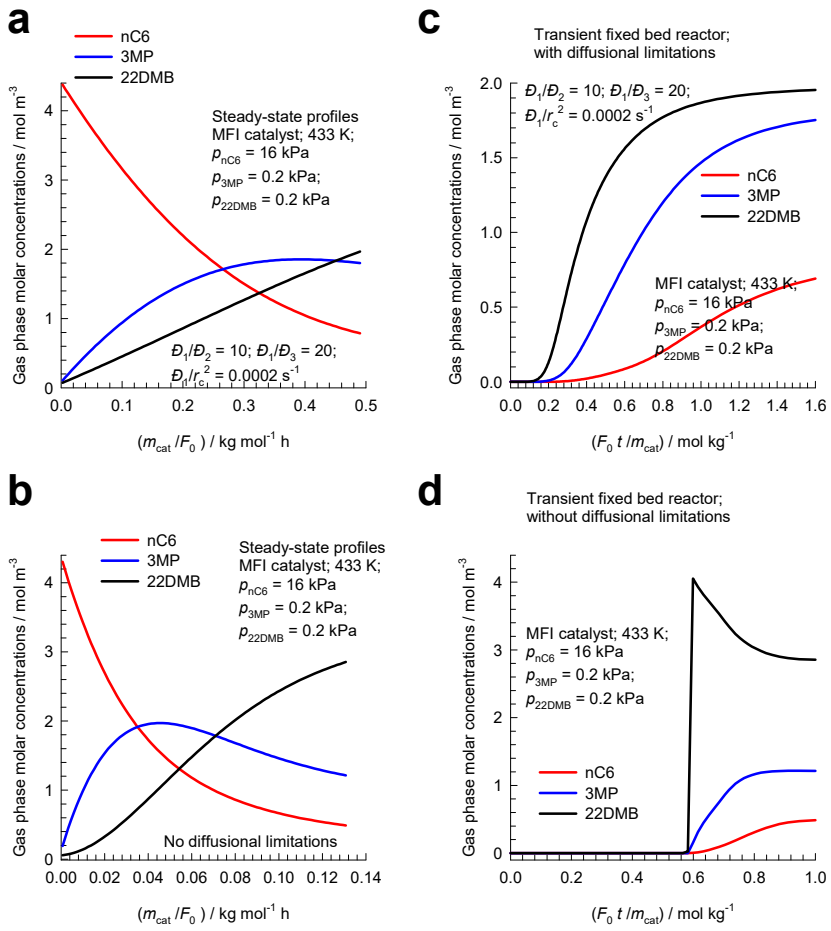

Figure S16. (a, b, c, d) Simulations of fixed bed reactor packed with MFI catalyst exposed to a gas phase nC6(1)/3MP(2)/22DMB(3) mixture at 433 K, carrying out the isomerization reaction $\text{nC6(1)} \rightleftarrows \text{3MP(2)} \rightleftarrows \text{22DMB(3)}$. The partial pressures of the components in the bulk gas phase at the reactor inlet are p_1 = 10 kPa; p_2 = 0.2 kPa, p_3 = 0.2 kPa. In (a, b) the steady-state composition profiles are shown. In (c, d) the transient compositions exiting the fixed bed reactor are presented. In the simulations (b, d) the intra-crystalline diffusional effects are ignored.

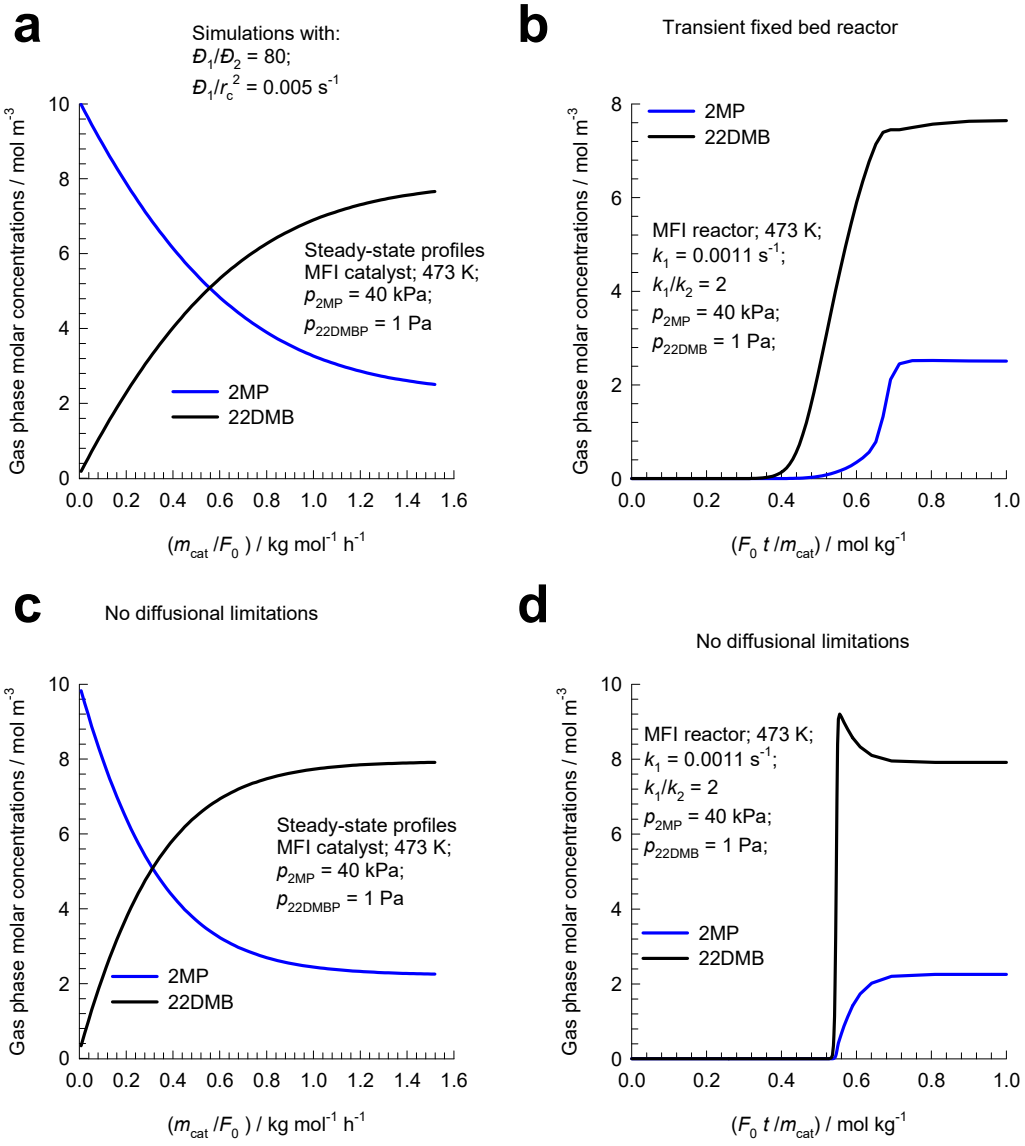

Figure S17. (a, b, c, d) Simulations of fixed bed reactor packed with MFI catalyst exposed to a gas phase 2MP(1)/22DMB(2) mixture at 473 K, carrying out the isomerization reaction $2MP(1) \rightleftarrows 22DMB(2)$. The partial pressures of the components in the bulk gas phase at the reactor inlet are p_1 = 40 kPa; p_2 = 1 Pa. In (a, b) the steady-state composition profiles are shown. In (c, d) the transient compositions exiting the fixed bed reactor are presented. In the simulations (b, d) the intra-crystalline diffusional effects are ignored. The input data for isotherms, diffusivities, and reaction rate constants are provided in Table S2.

6 Nomenclature

Latin alphabet

b_i	Langmuir parameter, Pa^{-1}
c_i	molar concentration of species *i*, mol m^{-3}
c_t	total molar concentration in mixture, mol m^{-3}
$Đ_i$	Maxwell-Stefan diffusivity for molecule-wall interaction, m^2 s^{-1}
$Đ_{ij}$	M-S exchange coefficient for *n*-component mixture, m^2 s^{-1}
f_i	partial fugacity of species *i*, Pa
F_0	molar flow rate of gas mixture entering fixed bed, mol s^{-1}
m_{cat}	mass of adsorbent packed in fixed bed, kg
n	number of species in the mixture, dimensionless
L	length of packed bed adsorber, m
N_i	molar flux of species *i* with respect to framework, mol m^{-2} s^{-1}
p_i	partial pressure of species *i* in mixture, Pa
p_t	total system pressure, Pa
q_i	component molar loading of species *i*, mol kg^{-1}
$q_{i,sat}$	molar loading of species *i* at saturation, mol kg^{-1}
q_t	total molar loading in mixture, mol kg^{-1}
$\bar{q}_i(t)$	radial-averaged component loading of species *i*, mol kg^{-1}
r	radial direction coordinate, m
r_c	radius of crystallite, m
R	gas constant, 8.314 J mol^{-1} K^{-1}
R_{kg}	rate of chemical reaction, mol (kg catalyst)$^{-1}$ s^{-1}
t	time, s

T	absolute temperature, K
u_i	velocity of motion of adsorbate species *i* with respect to the framework material, m s^{-1}
u	superficial gas velocity in packed bed, m s^{-1}
v	interstitial gas velocity in packed bed, m s^{-1}
x_i	mole fraction of species *i* in adsorbed phase, dimensionless
z	distance along the adsorber, m

Greek alphabet

Γ_{ij}	thermodynamic factors, dimensionless
δ_{ij}	Kronecker delta, dimensionless
ε	voidage of packed bed, dimensionless
θ_i	fractional occupancy of component *i*, dimensionless
θ_t	fractional occupancy of adsorbed mixture, dimensionless
θ_V	fractional vacancy, dimensionless
μ_i	molar chemical potential, J mol^{-1}
ν_i	stoichiometric reaction coefficient, dimensionless
ν	Freundlich exponent, dimensionless
ρ	framework density, kg m^{-3}

Subscripts

b	referring to backward reaction
c	referring to crystallite
f	referring to forward reaction
i	referring to component *i*

sat	referring to saturation conditions
t	referring to total mixture
V	vacancy

7 References

(1) Krishna, R. Tracing the Origins of Transient Overshoots for Binary Mixture Diffusion in Microporous Crystalline Materials. *Phys. Chem. Chem. Phys.* **2016**, *18*, 15482-15495. https://doi.org/10.1039/C6CP00132G.

(2) Krishna, R. A Maxwell-Stefan-Glueckauf Description of Transient Mixture Uptake in Microporous Adsorbents. *Sep. Purif. Technol.* **2018**, *191*, 392-399. https://doi.org/10.1016/j.seppur.2017.09.057.

(3) Krishna, R. Highlighting the Influence of Thermodynamic Coupling on Kinetic Separations with Microporous Crystalline Materials. *ACS Omega* **2019**, *4*, 3409-3419. https://doi.org/10.1021/acsomega.8b03480.

(4) Krishna, R. The Maxwell-Stefan Description of Mixture Diffusion in Nanoporous Crystalline Materials. *Microporous Mesoporous Mater.* **2014**, *185*, 30-50. https://doi.org/10.1016/j.micromeso.2013.10.026.

(5) Krishna, R.; van Baten, J. M. Maxwell-Stefan modeling of slowing-down effects in mixed gas permeation across porous membranes. *J. Membr. Sci.* **2011**, *383*, 289-300. https://doi.org/10.1016/j.memsci.2011.08.067.

(6) Myers, A. L.; Prausnitz, J. M. Thermodynamics of Mixed Gas Adsorption. *A.I.Ch.E.J.* **1965**, *11*, 121-130.

(7) Siperstein, F. R.; Myers, A. L. Mixed-Gas Adsorption. *A.I.Ch.E.J.* **2001**, *47*, 1141-1159.

(8) Streb, A.; Mazzotti, M. Adsorption for efficient low carbon hydrogen production: part 1—adsorption equilibrium and breakthrough studies for $H_2/CO_2/CH_4$ on zeolite 13X. *Adsorption* **2021**, *27*, 541-558. https://doi.org/10.1007/s10450-021-00306-y.

(9) Krishna, R.; Van Baten, J. M. Using Molecular Simulations to Unravel the Benefits of Characterizing Mixture Permeation in Microporous Membranes in Terms of the Spreading Pressure. *ACS Omega* **2020**, *5*, 32769−32780. https://dx.doi.org/10.1021/acsomega.0c05269.

(10) Krishna, R.; Van Baten, J. M. Elucidation of Selectivity Reversals for Binary Mixture Adsorption in Microporous Adsorbents. *ACS Omega* **2020**, *5*, 9031-9040. https://doi.org/10.1021/acsomega.0c01051.

(11) Krishna, R.; Van Baten, J. M. Using Molecular Simulations for Elucidation of Thermodynamic Non-Idealities in Adsorption of CO_2-containing Mixtures in NaX Zeolite. *ACS Omega* **2020**, *5*, 20535-20542. https://doi.org/10.1021/acsomega.0c02730.

(12) Krishna, R.; Van Baten, J. M. Water/Alcohol Mixture Adsorption in Hydrophobic Materials: Enhanced Water Ingress caused by Hydrogen Bonding. *ACS Omega* **2020**, *5*, 28393-28402. https://doi.org/10.1021/acsomega.0c04491.

(13) Krishna, R.; Van Baten, J. M. Investigating the Non-idealities in Adsorption of CO_2-bearing Mixtures in Cation-exchanged Zeolites. *Sep. Purif. Technol.* **2018**, *206*, 208-217. https://doi.org/10.1016/j.seppur.2018.06.009.

(14) Ruthven, D. M. *Principles of Adsorption and Adsorption Processes*. John Wiley: New York, 1984.

(15) Kooijman, H. A.; Taylor, R. A dynamic nonequilibrium model of tray distillation columns. *A.I.Ch.E.J.* **1995**, *41*, 1852-1863.

(16) Michelsen, M. An efficient general purpose method of integration of stiff ordinary differential equations. *A.I.Ch.E.J.* **1976**, *22*, 594-597.

(17) Bulirsch, R.; Stoer, J. Numerical treatment of ordinary differential equations by extrapolation methods. *Numer. Math.* **1966**, *8*, 1-14.

(18) Krishna, R.; Baur, R. Modelling Issues in Zeolite Based Separation Processes. *Sep. Purif. Technol.* **2003**, *33*, 213-254.

(19) Krishna, R.; Baur, R. Diffusion, Adsorption and Reaction in Zeolites: Modelling and Numerical Issues. http://krishna.amsterchem.com/zeolite/, University of Amsterdam, Amsterdam, 1 January 2015.

(20) Krishna, R.; van Baten, J. M. Investigating the potential of MgMOF-74 membranes for CO_2 capture. *J. Membr. Sci.* **2011**, *377*, 249-260.

(21) He, Y.; Krishna, R.; Chen, B. Metal-Organic Frameworks with Potential for Energy-Efficient Adsorptive Separation of Light Hydrocarbons. *Energy Environ. Sci.* **2012**, *5*, 9107-9120.

(22) Krishna, R. Screening Metal-Organic Frameworks for Mixture Separations in Fixed-Bed Adsorbers using a Combined Selectivity/Capacity Metric. *RSC Adv.* **2017**, *7*, 35724-35737. https://doi.org/10.1039/C7RA07363A.

(23) Krishna, R. Methodologies for Evaluation of Metal-Organic Frameworks in Separation Applications. *RSC Adv.* **2015**, *5*, 52269-52295. https://doi.org/10.1039/C5RA07830J.

(24) Krishna, R.; Baur, R.; Van Baten, J. M. Highlighting Diffusional Coupling Effects in Zeolite Catalyzed Reactions by Combining the Maxwell-Stefan and Langmuir-Hinshelwood Formulations. *React. Chem. Eng.* **2017**, *2*, 324-336.

(25) Ruthven, D. M.; Farooq, S.; Knaebel, K. S. *Pressure swing adsorption*. VCH Publishers: New York, 1994.

(26) Tester, J. W.; Modell, M. *Thermodynamics and its Applications*. 3rd Edition, Prentice Hall, Inc.: Upper Saddle River, NJ, USA, 1997.

(27) Sandler, S. I. *Chemical, Biochemical, and Engineering Thermodynamics*. 3rd Edition, John Wiley: New York, 1999.

(28) Krishna, R. Elucidation and Characterization of Entropy Effects in Mixture Separations with Micro-porous Crystalline Adsorbents. *Sep. Purif. Technol.* **2019**, *215*, 227-241. https://doi.org/10.1016/j.seppur.2019.01.014.

(29) Vlugt, T. J. H.; Zhu, W.; Kapteijn, F.; Moulijn, J. A.; Smit, B.; Krishna, R. Adsorption of linear and branched alkanes in the silicalite-1. *J. Am. Chem. Soc.* **1998**, *120*, 5599-5600.

(30) Vlugt, T. J. H.; Krishna, R.; Smit, B. Molecular Simulations of Adsorption Isotherms for Linear and Branched Alkanes and Their Mixtures in Silicalite. *J. Phys. Chem. B* **1999**, *103*, 1102-1118.

(31) Krishna, R.; Smit, B.; Calero, S. Entropy effects during sorption of alkanes in zeolites. *Chem. Soc. Rev.* **2002**, *31*, 185-194.

(32) Schenk, M.; Vidal, S. L.; Vlugt, T. J. H.; Smit, B.; Krishna, R. Separation of alkane isomers by exploiting entropy effects during adsorption on silicalite-1: A configurational-bias Monte Carlo simulation study. *Langmuir* **2001**, *17*, 1558-1570.

(33) Calero, S.; Smit, B.; Krishna, R. Configurational entropy effects during sorption of hexane isomers in silicalite. *J. Catal.* **2001**, *202*, 395-401.

(34) Titze, T.; Chmelik, C.; Kärger, J.; van Baten, J. M.; Krishna, R. Uncommon Synergy Between Adsorption and Diffusion of Hexane Isomer Mixtures in MFI Zeolite Induced by Configurational Entropy Effects *J. Phys. Chem. C* **2014**, *118*, 2660-2665. https://doi.org/10.1021/jp412526t.

(35) Krishna, R.; van Baten, J. M. Investigating the Relative Influences of Molecular Dimensions and Binding Energies on Diffusivities of Guest Species Inside Nanoporous Crystalline Materials *J. Phys. Chem. C* **2012**, *116*, 23556-23568. https://doi.org/10.1021/jp308971w.

(36) Krishna, R.; van Baten, J. M. Influence of Adsorption Thermodynamics on Guest Diffusivities in Nanoporous Crystalline Materials. *Phys. Chem. Chem. Phys.* **2013**, *15*, 7994-8016.

(37) Schuring, D.; Jansen, A. P. J.; van Santen, R. A. Concentration and chainlength dependence of the diffusivity of alkanes in zeolites studied with MD simulations. *J. Phys. Chem. B* **2000**, *104*, 941-948.

(38) Krishna, R.; van Baten, J. M. Diffusion of Hydrocarbon Mixtures in MFI Zeolite: Influence of Intersection Blocking. *Chem. Eng. J.* **2008**, *140*, 614-620.

(39) Cavalcante, C. L.; Ruthven, D. M. Adsorption of Branched and Cyclic Paraffins in Silicalite .2. Kinetics. *Ind. Eng. Chem. Res.* **1995**, *34*, 185-191.

(40) Jolimaître, E.; Tayakout-Fayolle, M.; Jallut, C.; Ragil, K. Determination of mass transfer and thermodynamic properties of branched paraffins in silicalite by inverse chromatography technique. *Ind. Eng. Chem. Res.* **2001**, *40*, 914-926.

(41) Krishna, R.; Baur, R. On the Langmuir-Hinshelwood formulation for zeolite catalysed reactions. *Chem. Eng. Sci.* **2005**, *60*, 1155 - 1166.

(42) Herm, Z. R.; Wiers, B. M.; Van Baten, J. M.; Hudson, M. R.; Zajdel, P.; Brown, C. M.; Maschiocchi, N.; Krishna, R.; Long, J. R. Separation of Hexane Isomers in a Metal-Organic Framework with Triangular Channels *Science* **2013**, *340*, 960-964. https://www.science.org/doi/10.1126/science.1234071.

(43) Krishna, R. Diffusing Uphill with James Clerk Maxwell and Josef Stefan. *Chem. Eng. Sci.* **2019**, *195*, 851-880. https://doi.org/10.1016/j.ces.2018.10.032.

(44) Krishna, R. Uphill Diffusion in Multicomponent Mixtures. *Chem. Soc. Rev.* **2015**, *44*, 2812-2836. https://doi.org/10.1039/C4CS00440J.

(45) Baur, R.; Krishna, R. Effectiveness factor for zeolite catalysed isomerization reactions. *Chem. Eng. J.* **2004**, *99*, 105-116.

(46) Krishna, R.; van Baten, J. M. In silico screening of metal-organic frameworks in separation applications. *Phys. Chem. Chem. Phys.* **2011**, *13*, 10593-10616. https://doi.org/10.1039/C1CP20282K.

(47) Krishna, R. Maxwell-Stefan Modelling of Mixture Desorption Kinetics in Microporous Crystalline Materials. *Sep. Purif. Technol.* **2019**, *229*, 115790. https://doi.org/10.1016/j.seppur.2019.115790.